

**$v_2$  calculation for  $h$ ,  $\pi$ ,  $p$  and  $K$  in p-Pb collisions at  
 $\sqrt{S_{NN}} = 5.02$  TeV, using the Scalar Product**

Mathias Veenman  
3349357  
Institute for Subatomic Physics  
Utrecht University

*Supervised by:*  
Prof. dr. R. Snellings  
A. Dubla  
A. F. Dobrin

January 14, 2014

## Abstract

The target of this thesis is to measure the elliptic flow  $v_2$  in p-Pb collisions using the data collected from the ALICE experiment in 2013. Elliptic flow in Pb-Pb is observed and is important for research in Quark Gluon Plasma (QGP), a new stage of matter created at very high energy density ( $\epsilon \sim 1 \text{ GeV}/\text{fm}^3$ ) and temperatures ( $T \sim 10^{15} \text{ K}$ ). This collective expansion was also already measured in p-Pb collisions using 2-Particle Correlation by ALICE experiment[5]. This thesis used a different method to extract the  $v_2$ : the Scalar Product.

The elliptic flow in the first part of this thesis is studied for charged particles. In the second part particle identification studies are reported for  $\pi$ , K, p respectively. A subtraction had been done between the (0-20%) and (60-100%) multiplicity bins to remove non-flow effects and the  $v_2$  coefficient for charged particles and the particle species is reported.

# Contents

<b>1</b>	<b>Intro</b>	<b>4</b>
1.1	Introduction to flow . . . . .	4
1.2	Elliptic flow . . . . .	5
<b>2</b>	<b>Detectors</b>	<b>5</b>
2.1	Inner Tracking System . . . . .	5
2.2	Time Projection Chamber . . . . .	6
2.3	Time Of Flight . . . . .	7
2.4	VZERO . . . . .	7
2.5	Event and track selection . . . . .	8
<b>3</b>	<b>Methods</b>	<b>10</b>
3.1	Proton-Lead . . . . .	10
3.2	2 -Particle correlation . . . . .	10
3.3	Scalar Product . . . . .	10
3.3.1	Results Scalar Product . . . . .	11
3.3.2	Subevents . . . . .	12
3.3.3	$\eta$ -gap . . . . .	12
3.4	Non Uniform Acceptance-correction . . . . .	13
3.5	Multiplicity bin subtraction . . . . .	15
3.5.1	Results . . . . .	17
3.6	Particle Identification . . . . .	17
3.6.1	PID using TPC . . . . .	18
3.6.2	PID using TOF . . . . .	19
3.6.3	Combining and selecting . . . . .	20
3.6.4	Results PID . . . . .	20
3.6.5	Further checks on PID at high $p_T$ . . . . .	21
3.6.6	NUA-correction for particles . . . . .	22
3.6.7	Subtraction for particles species . . . . .	26
3.6.8	Results subtraction PID . . . . .	26
<b>4</b>	<b>Conclusion</b>	<b>27</b>
	<b>References</b>	<b>28</b>

# 1 Intro

The ALICE Detector (A Large Ion Collision Experiment) is built to study a new state of matter which exist at very high energy density ( $\epsilon \sim 1 \text{ GeV}/\text{fm}^3$ ) and temperatures ( $T \sim 10^{15} \text{ K}$ ). It is called Quark Gluon Plasma (QGP) and is predicted by Quantum Chromodynamics (QCD). The interest for this new phase is because the early universe is believed to behave as the QGP. For example, the hot and dense matter involved in a heavy ion collision will also expand and cool down, just like the early universe. During this expansion the system has a range of temperatures and energy densities and finally hadronizes. The collective expansion that happens in these conditions is called flow.

There are still a lot of fundamental questions left to be answered, and the QGP created inside heavy ion collisions hopefully can answer some. The QGP cannot be studied directly, but it can be examined in other ways. Different methods are available, such as strangeness production, jet quenching and heavy flavour suppression. This thesis is focused on the previously described collective expansion of the system after the collision.

## 1.1 Introduction to flow

When two heavy ions hit each other in the Large Hadron Collider (LHC) it will most likely not be a head-on collision. This has as effect that the overlapping volume has an almond shape form, instead of a circular. The latter would have been the case if the collision was perfectly head-on. This is visually shown in figure 1. The impact parameter  $b$  is the parameter describing the distance between the two centres of the colliding ions. The larger this parameter is, that means that the collision is less central, the larger the eccentricity of the almond shape. If the parameter  $b$  is zero, then the collision is almost head-on, and the almond shape has a very small eccentricity.

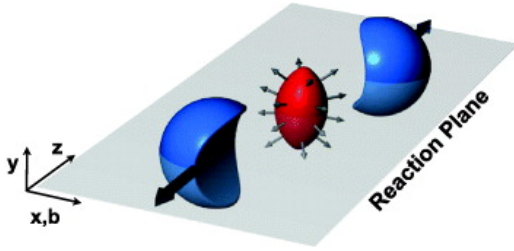


Figure 1: The overlapping volume in a non-central heavy ion collision [2]

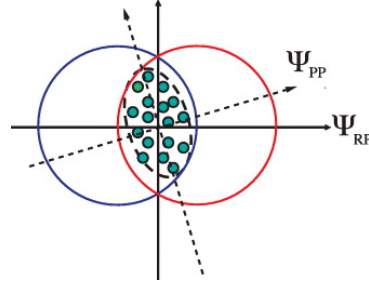


Figure 2: Difference between the Reaction plane and the Participant plane [2]

This has as effect that the particle distribution is correlated with respect to the reaction plane. The reaction plane is spanned by the beam direction  $z$  and the impact parameter. But not all particles inside the overlapping volume do participate in the collision. For example, some particles from one of the ions could miss all of the particles from the other ion. Therefore there is another plane, which is more important than the reaction plane. It is called the participant plane, and is spanned by the short axis of the participant volume and the beam axis. The difference between the reaction plane and the participant plane is shown in figure 2. The best way to describe the anisotropic particle distribution in the participant plane is with a Fourier expansion of the differential distribution of particles:

$$E \frac{d^3 N}{d^3 p} = \frac{d^3 N}{p_T dp_T d\eta d[\phi - \Psi_{RP}]} = \frac{1}{2\pi} \frac{d^2 N}{p_T dp_T d\eta} \left( 1 + \sum_{n=1}^{\infty} 2v_n(p_T, \eta) \cos[n(\phi - \Psi_{RP})] \right) \quad (1)$$

Where  $E$  is the energy of the particle,  $p$  the momentum,  $p_T$  the transverse momentum,  $\eta$  the rapidity,  $\phi$  the azimuthal angle,  $\Psi_{RP}$  the angle of the reaction plane and  $v_n$  the flow coefficients.

The Fourier coefficients are the most interesting parts. They are  $p_T$  and  $\eta$  dependant and given by:

$$v_n(p_T, \eta) = \langle \cos[n(\phi - \Psi_{RP})] \rangle \quad (2)$$

The angular brackets denote an average over all the particles, in all events, in the current  $(p_T, \eta)$ -bin. The first two coefficients,  $v_1$  and  $v_2$ , are respectively known as directed and elliptic flow. Directed flow is an effect due to the motion of the nucleons of the ions that have not interacted, called spectators. Elliptic flow is coming from the expansion of the almond shaped active medium and interactions between the participant particles.

## 1.2 Elliptic flow

Elliptic flow has been calculated in Pb-Pb system for charged particles [3] and different species [4] by the ALICE collaboration. In figure 3 and 4 the results for charged particles and different species are shown respectively. We see an increasing elliptic flow, up to  $p_T \sim 3$  GeV/c, from where the  $v_2$  slightly decreases. For different particle species we see two more effects, namely mass scaling and proton crossover.

To look if there is also elliptic flow present in p-Pb systems, there has also been research done in that field and the results are shown in figure 5 [5]. From this picture we observe similar behaviour as in Pb-Pb collisions.

The mass scaling and proton crossover should help in the interpretation of the final results. Mass scaling that is visible at low  $p_T$  means that the particles which have a higher mass, have a lower elliptic flow. This is predicted by hydrodynamic model calculations because it costs more energy to push heavier particles a certain direction. This effect is visible in both Pb-Pb and p-Pb until a  $p_T$  of 2.5 GeV/c. The heaviest particle that was included in the analysis was the proton, with a mass of 938 MeV/c<sup>2</sup>. The Kaons are almost a factor 2 lighter, with a mass of 494 MeV/c<sup>2</sup>. The pions are the lightest, with a mass of 140 MeV/c<sup>2</sup>. The proton crossover means that at higher  $p_T$  proton has a higher elliptic flow than pion. Results from previous experiments and theoretical models we expect at high  $p_T$  a baryon-meson scaling which explains this effect.

The main goal in this thesis is to study the  $v_2$ -coefficients in p-Pb, but using a different method: the scalar product instead of the 2-Particle correlation.

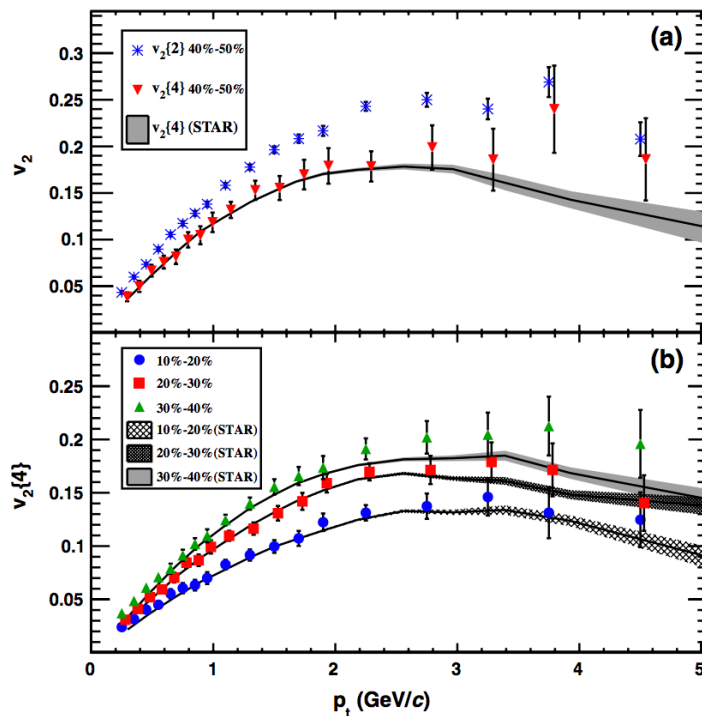


Figure 3: Results of the ALICE collaboration on the elliptic flow measurements in Pb-Pb collisions for charged particles only [3]. In the upper panel the difference between the  $v_2\{2\}$  and  $v_2\{4\}$  is shown. The  $v_2\{2\}$  is shown in blue star markers, and the  $v_2\{4\}$  in red triangles. In the lower panel the results of  $v_2\{4\}$  in different centrality bins is shown in comparison to RHIC experiments. The blue circle markers represent the (10-20%) centrality bin, in red squared markers the (20-30%) bin and the green triangle markers the (30-40%) bin.

## 2 Detectors

There are many detectors used in the ALICE experiment. A sketch of the detector with the different subdetectors is shown in figure 6. In the next subsections we will discuss the subdetectors used in this thesis used for tracking, particle identification and multiplicity determination.

### 2.1 Inner Tracking System

This is the first detector a particle passes through when it is coming from the collision. The outer dimensions are a length of 97.6 cm and a radius of 44 cm. It consists of six layers of silicon detectors including two Silicon Pixel Detectors (SPD), two Silicon Drift Detectors (SDD) and two Silicon Strip Detectors (SSD). Those are located at radii,  $r = 4, 7, 15, 24, 39$  and 44 cm. The ITS covers a pseudo-rapidity region of  $|\eta| < 0.9$ . It

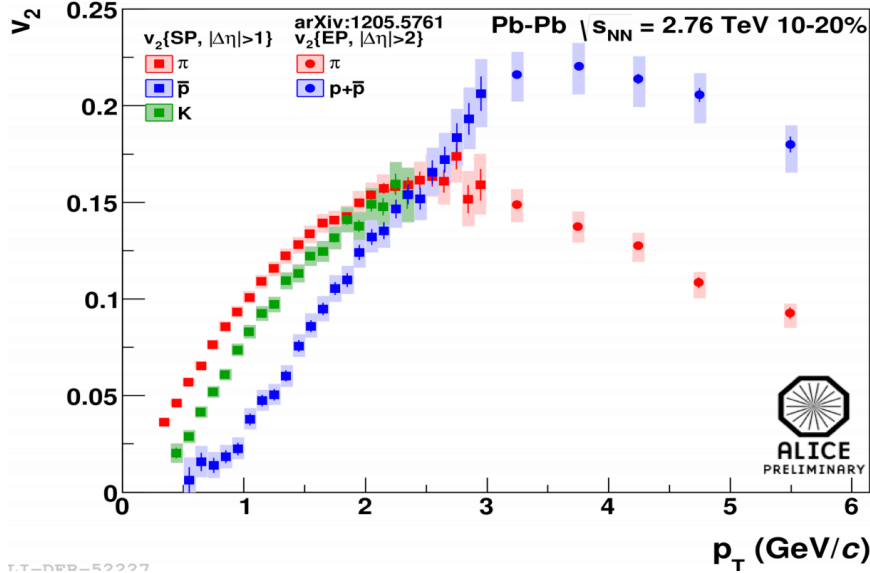


Figure 4: Results of the ALICE collaboration on the elliptic flow measurements in Pb-Pb collisions for different species [4]. The red, blue and green markers represent the pion, proton and kaon respectively.

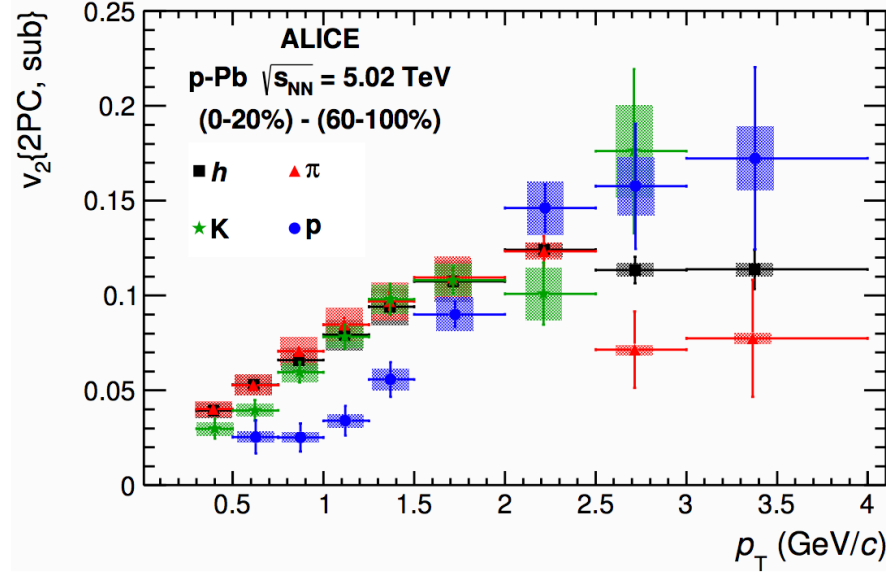


Figure 5: Results of the ALICE collaboration on the elliptic flow calculation in p-Pb collisions [5]. The black square, red triangle, blue circle and green star markers represent the charged particles, pion, proton and kaon respectively.

can calculate the primary vertex with a resolution better than  $100\mu m$ . It is also used to help reconstruct all tracks with high precision. Due to this high precision, decaying D and B mesons can be identified and particles coming from this decay can be removed to remove fake correlation. The ITS is also the only detector in ALICE that is able to measure particles with a  $p_T < 100$  MeV/c, but they are not used in this research.

## 2.2 Time Projection Chamber

When a charged particle passes through the gas in the TPC, it leaves a trail of ionized gas. This gas is transported away from the middle, to the side due to the electric field, where the readout-chambers are located. Those consist of wire planes and 560.000 electronic channels. and can detect the 3D-path and ionization density. The curvature of the path along with the magnetic field is used to calculate the velocity. The ionization density is used to determine the energy of the incoming particle, which is in turn used for  $dE/dx$ , energy loss per distance, computation. The  $dE/dx$  is very useful for particle identification, which will be explained in section 3.6.

For this research the TPC is used in track reconstruction combined with the ITS, momentum determination and particle identification through the  $dE/dx$ .

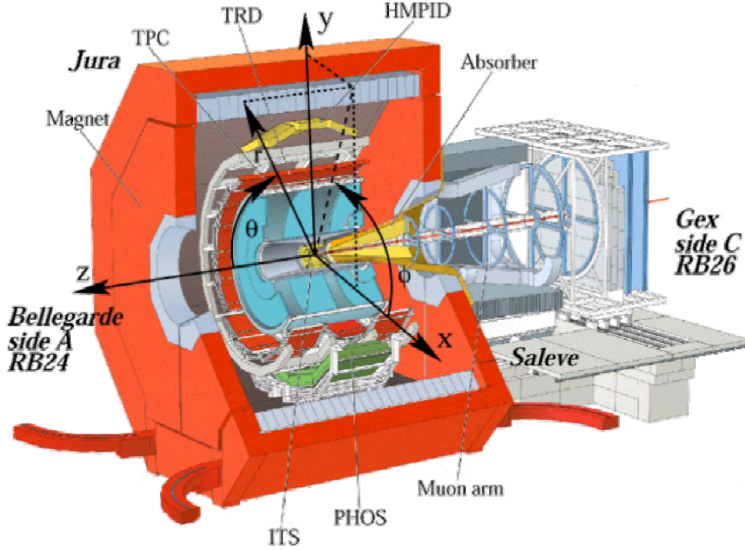


Figure 6: Overview of the ALICE detector with multiple detectors labeled. [8]

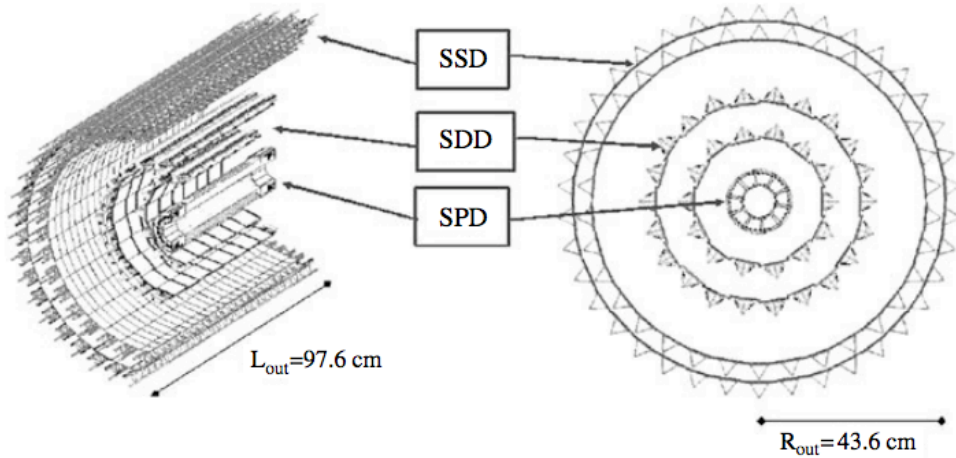


Figure 7: Overview of the ITS detector in ALICE [1]

## 2.3 Time Of Flight

The next detector is the Time of Flight detector (TOF) [10]. The detector covers a cylindrical surface with a polar acceptance of  $|\theta - 90^\circ| < 45^\circ$ . It is located at a radius between 3.70 and 3.99m. The detector consist of multiple Multi-gap Resistive-Plate Chamber (MRPC) strips, which are 1220 mm long and 130 mm wide. The active area is smaller, only 1200 by 74 mm. Inside each strip there are 96 readout pads, with a surface of  $3.5 \times 2.5 \text{ cm}^2$ . There are 1638 strips and 157248 pads in total.

In each working pad there are several layers of resistive glass with a gas mixture in between. A high voltage is applied on the pickup cathodes. When a charged particles flies through the gas, it ionises the gas, and the voltage difference starts an electron avalanche. The resistive layers are transparent for the fast signals created by the avalanches, and these signals are picked by the pick-up electrodes. This is visually shown in figure 9. The time difference between the kathode and the anode is converted into the time of flight of the particle.

## 2.4 VZERO

The VZERO detector is not a traditional detector in shape. It is divided into two large arrays located at 340 cm after the primary vertex (VZERO-A) and 90 cm behind it (VZERO-C). The VZERO-A spans a pseudorapidity of  $2.8 < \eta < 5.1$  and the VZERO-C  $-3.7 < \eta < -1.7$ . Both have 32 scintillator counters, separated in eight sectors of  $45^\circ$  and four rings, with a pseudorapidity coverage between  $0.4 - 0.6$ . The



Figure 8: A single strip of the ALICE TOF detector [1]

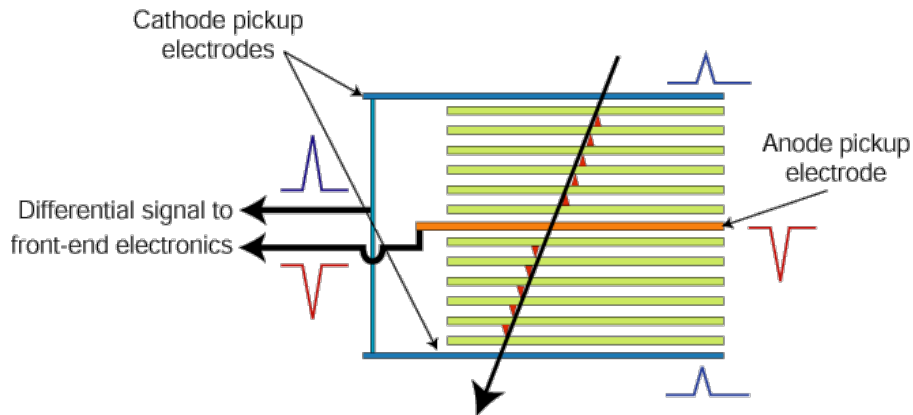


Figure 9: Working principle of the TOF-detector [11]

VZERO detector has multiple purposes but the one directly used in this thesis is the centrality or multiplicity determination. The centrality is taken from the VZERO-A detector. Due to lower correlation between centrality determination and number of tracks, the centrality determination is a delicate task in p-Pb. This correlation is shown for both p-Pb and Pb-Pb in figure 10 in the left and right panel respectively. We can clearly see that the correlation in p-Pb is much lower with respect to Pb-Pb. Therefore there is an overlap in track multiplicity for different multiplicity bins. This is shown in figure 11.

## 2.5 Event and track selection

The used data is from the ALICE detector, collected in 2013. There are  $102 \cdot 10^6$  events in this data. All tracks in each event coming from these detectors are subjected to filtering, to avoid tracks with bad quality. For example, a track with a pseudorapidity  $\eta > 0.8$  is rejected, because the Time Projection Chamber is known to not work very well at  $0.8 < \eta < 0.9$  due to edge effects. Above  $\eta = 0.9$  the detector does not measure at all anymore because there is no coverage.

The list of conditions the event has to satisfy before accepted:

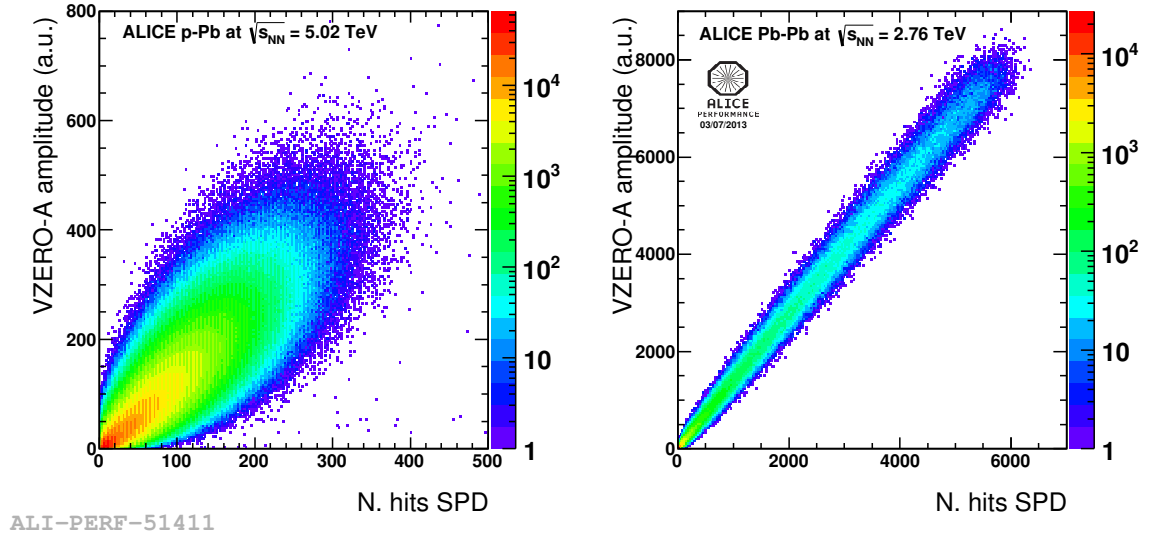


Figure 10: Correlation between centrality determination and multiplicity. In the left panel this correlation is shown for p-Pb collisions, in the right panel for Pb-Pb collisions. [12]

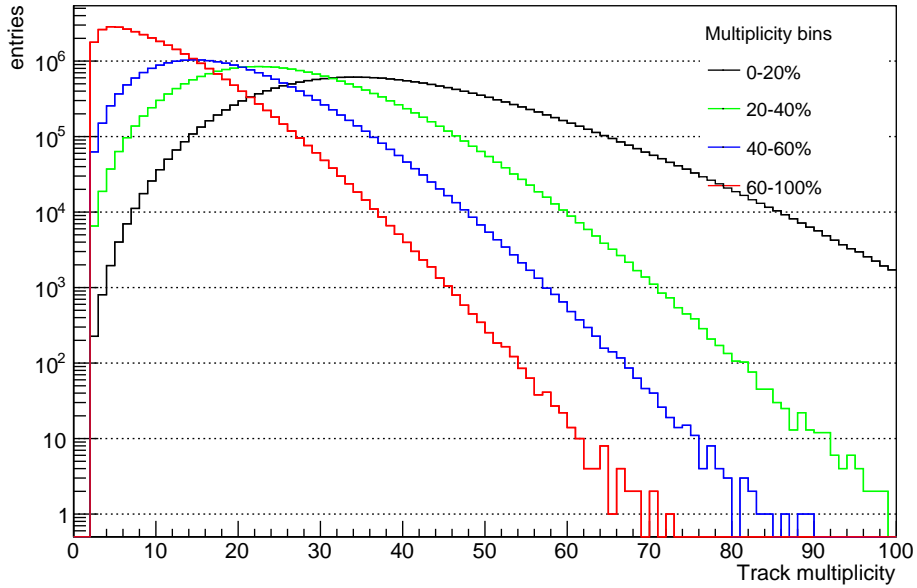


Figure 11: Multiplicity distribution for different multiplicity bins

- Amount of tracks  $> 2$
- $M_a > 1$  (amount of accepted tracks with negative  $\eta$ )
- $M_b > 1$  (amount of accepted tracks with positive  $\eta$ )

This is not very long, and is only based on the amount of accepted tracks. The list of conditions each tracks has to satisfy is quite larger.

- $0.2 < p_T < 20$
- $|\eta| < 0.8$
- $dE/dx > 10$
- Amount of clusters ( $ncl$ )  $> 70$
- Amount of clusters to reproduce the track ( $ncls$ )  $> 90$
- $TPC_{\chi^2} < 3.5$
- Filterbit = 256 or Filterbit = 512

The  $p_T$ ,  $\eta$  and  $dE/dx$  are to make sure that all tracks are well measured by the ALICE apparatus. The detectors will not work properly at a higher  $\eta$  for example. The data can become biased and that is why tracks that do not qualify are rejected.

The next three conditions are needed in order to use only tracks with good quality to reconstruct a good track. If there are less clusters used in the reconstruction, the probability to increase that the reproduced track is not exactly the same as the original one. The  $TPC\chi_2$  is the degree of accuracy of the tracking in the TPC. The lower it is, the better the track fits with the hits from the detectors.

Finally, the filterbit is a flag that is applied at tracks depending where the particle is originated. The filterbits 256 + 512 are applied to tracks coming from the primary collision. Tracks coming from decays have a different kinematic and they are excluded from the analysis. Every other track is coming from effects such as decay.

## 3 Methods

### 3.1 Proton-Lead

In the previous sections we gave a brief introduction on the elliptic flow in Pb-Pb and the detectors in the ALICE experiment. This thesis investigates proton-lead (p-Pb) collisions, which has slightly different physics. Instead of an overlapping volume of the colliding ions and interacting protons and neutrons from both ions, there is a relative small object (the proton) flying through an ion, and colliding with protons and neutrons of the lead ion. The spectator parts of the ions which normally cause directed flow ( $v_1$ ) which is observed in heavy ion collisions are absent. There is also no almond shape that expands which is one of the main reasons of elliptic flow ( $v_2$ ). However there are also similarities. The centrality/multiplicity dependence is still there for example. When the proton hits the lead ion in the middle, it will interact with many nucleons of the ion, while it is only a small fraction at the side. This centrality is reproduced by the VZERO detector, explained in section 2.4. The track multiplicity distribution for different centralities is previously shown in figure 11. Because centrality is not defined in p-Pb collisions, this study is done in multiplicity bins instead of centrality bins.

It is still interesting to look at the elliptic flow in p-Pb-collisions, because there could be enough interaction between particles to create elliptic flow. The potential presence of elliptic flow is an indication of QGP, and that is why this thesis wants to confirm it.

### 3.2 2-Particle correlation

Normally the angle of the reaction plane is estimated using the Event Plane method in Pb-Pb for calculation of  $v_2$ . However, this angle is not an observable in p-Pb collisions, because it is not possible to define an event plane and the eccentricity of the collisions. There are no two big objects who hit each other which centres defines the impact parameter and thus the reaction plane. Instead there is the proton who penetrates the lead ion. So there are other methods needed to calculate the flow. One is the 2-particle correlation. In this method the azimuthal correlations between two different particles are used to determine the elliptic flow[2]:

$$\begin{aligned} v_2\{2\} &= \left\langle \left\langle e^{2i(\phi_1 - \phi_2)} \right\rangle \right\rangle = \left\langle \left\langle e^{2i(\phi_1 - \Psi_{RP} - (\phi_2 - \Psi_{RP}))} \right\rangle \right\rangle \\ &= \left\langle \left\langle e^{2i(\phi_1 - \Psi_{RP})} \right\rangle \left\langle e^{2i(\phi_2 - \Psi_{RP})} \right\rangle + \delta_2 \right\rangle \\ &= \langle v_2^2 + \delta_2 \rangle \end{aligned} \quad (3)$$

The 2-Particle correlation ( $v_2\{2\}$ ) is now split into two parts, the elliptic flow ( $v_2$ ) and non-flow correlations ( $\delta_2$ ). This can only be done if the correlation between  $v_2$  and  $\delta_2$  is small. If  $\delta_2$  is neglectable in respect to  $v_2$ , then this formula can be used to calculate  $v_2$ . Unfortunately, this is probably not a valid assumption in p-Pb, because there are a lot of non-flow correlations. For example the tracks of a jet fragmentation in a low multiplicity collision have a huge influence, but is not elliptic flow and probably  $\delta_2$  is not neglectable with respect to  $v_2$ . This method is used for the results for the elliptic flow in p-Pb collisions shown in figure 5. A different method is used in this thesis to calculate  $v_2$ . This is the scalar product and it also has the advantage that an  $\eta$ -gap can be applied to remove non-flow correlations. This method is explained in the next section.

### 3.3 Scalar Product

A quick introduction of this method is given in this section, alongside with the results obtained in this thesis. All results in this thesis are generated using the Scalar Product, reported in equation 4.

$$v_2 = \frac{\langle \langle uQ^* \rangle / M \rangle}{\sqrt{\langle \frac{Q_a Q_b^*}{M_a M_b} \rangle}} \quad (4)$$

Where  $u$  is the vector of the particle of interest,  $Q$  is the flow-vector in a single event,  $Q_a$  and  $Q_b$  are the flow-vectors of two different subevents,  $M$  is the total multiplicity, and  $M_a$  and  $M_b$  are the multiplicities of

the two subevents in a single event. The star (\*) indicates a complex conjugate, because the  $x$ -axis is taken to be real and the  $y$ -axis imaginary. This is only a notation we are using, and has no resemblance with the reality. The  $\langle \rangle$  brackets around  $uQ^*$  and  $Q_aQ_b^*$  denote an average over all the events. The numerator has two  $\langle \rangle$  brackets, and it should first be averaged over all the tracks in a single event, then averaged over all events. The different subevents are chosen to depend on the pseudorapidity  $\eta$  of the track reconstructed by the Time Projection Chamber. If the  $\eta$  is negative, the track comes in the  $a$ -side. If the  $\eta$  is positive, the track comes in the  $b$ -side.

The main idea of this method is to correlate each track with the average direction of all particles. In this part it differs from the 2-Particle correlation method, where each single track is correlated with all other tracks in the events.

The previously mentioned Q-vector is calculated by:

$$Q_x = \sum^{N_{particles}} \cos 2\phi_p \quad (5)$$

$$Q_y = \sum^{N_{particles}} \sin 2\phi_p \quad (6)$$

Where  $\phi_p$  is the  $phi$  (azimuthal) angle of a specific track in an event. The  $u$ -vector is simply:

$$u_x = \cos 2\phi \quad (7)$$

$$u_y = \sin 2\phi \quad (8)$$

The trick with the imaginary  $y$ -axis and the complex conjugate ensures the product of  $uQ^*$  is going well:

$$\langle uQ^* \rangle = (u_x + u_y)(Q_x + Q_y)^* \quad (9)$$

Fill these variables from equation 5, 6, 7 and 8 gives:

$$\langle uQ^* \rangle = (\cos 2\phi + i \sin 2\phi) \left( \sum_p^{N_{particles}} \cos 2\phi_p + i \sum_p^{N_{particles}} \sin 2\phi_p \right)^* \quad (10)$$

Multiplication gives the final result, which is used in the calculations. The imaginary parts are dropped out.

$$\cos 2\phi \sum_p^{N_{particles}} \cos 2\phi_p + \sin 2\phi \sum_p^{N_{particles}} \sin 2\phi_p \quad (11)$$

Note that there is only one Q-vector for each event, but every single track in an event has his own  $u$ -vector. Therefore the Q-vector has to be calculated before the  $\langle uQ^* \rangle$  part.

This method has also one big disadvantage: the  $u$ -vector is also in the summed Q-vector. Therefore there is always a small correlation with itself, called auto-correlation. This effect has to be removed and this is done by subtracting the  $u$ -vector from the Q-vector. The final equation for the numerator yields :

$$\langle uQ^* \rangle = \langle u(Q - u)^* \rangle = \cos 2\phi \left( \sum_p^{N_{particles}} \cos 2\phi_p - \cos 2\phi \right) + \sin 2\phi \left( \sum_p^{N_{particles}} \sin 2\phi_p - \sin 2\phi \right) \quad (12)$$

The calculation for the denominator goes similar:

$$\langle Q_a Q_b^* \rangle = \langle Q_{a,x} Q_{b,x} + Q_{a,y} Q_{b,y} \rangle \quad (13)$$

These values can be filled from equations 5 and 6, but only take the particles from the a or b side.

### 3.3.1 Results Scalar Product

The results obtained with this method are shown in figure 12 where the elliptic flow is plotted as a function of  $p_T$  for different multiplicity bins. The black full circle markers are the (0-20%) multiplicity bin. The green squared markers are the (20-40%) multiplicity bin. The blue triangle markers are the (40-60%) multiplicity bin. Finally, the red open circle markers are the (60-100%) multiplicity bin.

There is seen that the flow is increasing with higher  $p_T$ . The highest multiplicity bin (60-100%) returns to have the highest  $v_2$  values and lowest the multiplicity bin returns to have the lowest  $v_2$ . This is because the non-flow correlations are inversely proportional to the amount of tracks. The elliptic flow in p-Pb collisions is generated by interacted tracks, so the more tracks interact with each other, the higher the elliptic flow is. Non-flow correlation does not depend on the amount of tracks and can be for example present in the form of a jet. The track of jets do however have a much greater influence on the calculated flow in events with low multiplicity, because in that case lots of tracks in that kind of events are coming from jet fragmentation and not from global expansion. Therefore the events with the lowest multiplicity have the highest elliptic flow. In the next section we will discuss different ways to estimate and remove the non-flow correlation.

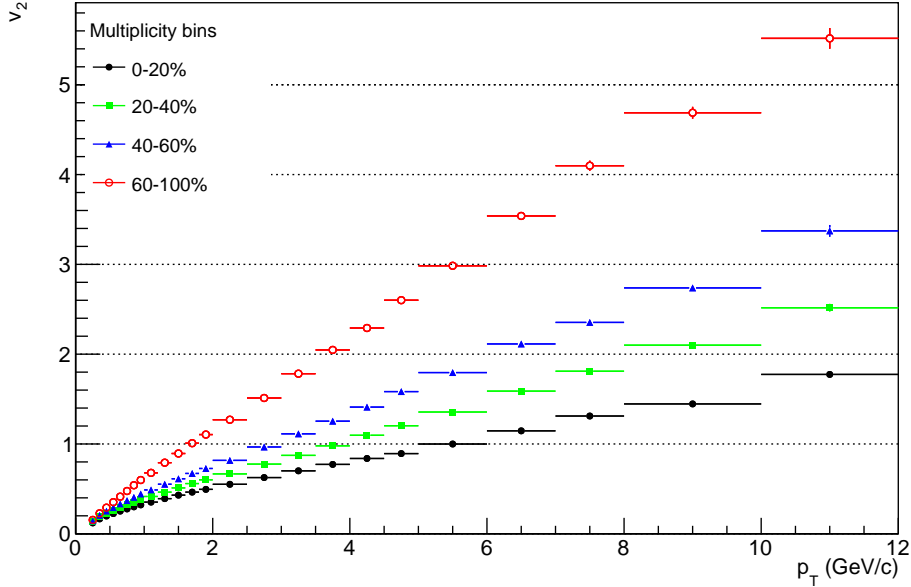


Figure 12: Elliptic flow results extracted using the Scalar Product method. The measurements are reported for different multiplicity bins.

### 3.3.2 Subevents

Another way to deal with the auto-correlation is to exploit the two subevents a little bit more. It is already explained that the  $Q_a$  and  $Q_b$  vectors were divided based on the  $\eta$ . The important new step is that also the  $Q$ -vector in the numerator is either  $Q_a$  or  $Q_b$ , depending from which side the  $u$ -vector is coming. The  $u$ -vector and  $Q$ -vector always come from the opposite sides. In this way the auto-correlation is automatically removed.

For example, imagine a collision with ten accepted tracks, from which four have a negative  $\eta$  and thus six a positive  $\eta$ . The  $Q_a$  vector consist of four particles and the  $Q_b$  vector of six. When the elliptic flow is calculated, every track acts once as the particle of interest (the  $u$ -vector). Four times a particle is in the  $a$ -side, and the flow of this particle is calculated with the  $Q$ -vector from the  $b$ -side ( $Q_b$ ). In the same way, there are six particles in the  $b$ -side, and the  $Q_a$ -vector is used in the flow calculation six times. The denominator will use the same  $Q_a$  and  $Q_b$ -vector.

The formula for the Scalar Product method with the use of different subevents is the following:

$$v_{2,a} = \frac{\langle\langle u_a Q_b^* \rangle\rangle / M_b}{\sqrt{\langle\langle \frac{Q_a Q_b^*}{M_a M_b} \rangle\rangle}} \quad (14)$$

$$v_{2,b} = \frac{\langle\langle u_b Q_a^* \rangle\rangle / M_a}{\sqrt{\langle\langle \frac{Q_a Q_b^*}{M_a M_b} \rangle\rangle}} \quad (15)$$

These can be combined by using the average mean and gives the final equation for the Scalar Product method. One should keep in mind that the  $u$ -vector and  $Q$ -vector should come from opposites sides. The multiplicity  $M$  is the amount of tracks that is used to construct the  $Q$ -vector and should therefor be from the same side as the  $Q$ -vector. This yields the same formula as equation 4.

### 3.3.3 $\eta$ -gap

There is also another huge advantage in this method with subevents. So far, the  $a$ -side and  $b$ -side consist tracks of  $\eta < 0$  and  $\eta > 0$  respectively. An  $\eta$ -gap can be introduced between the  $u$ -vector and  $Q$ -vector, so that only tracks with an absolute  $\eta$  larger then a certain value will be accepted then this will cause to reject all tracks with a low pseudorapidity. This  $\eta$ -gap is symmetrical and centralised at  $\eta = 0$ . An  $\eta$ -gap of 0.8 means that the removed tracks have an  $\eta$  of  $-0.4 < \eta < 0.4$ . The effect is that most jet contributions will be removed and therefor some non-flow correlation. The expectation is that the flow will decrease with a higher  $\eta$ -gap because increasing the  $\eta$ -gap will exclude more tracks coming from a jet.

However, there are also tracks excluded that are not coming from jet fragmentation because they can also have a small pseudorapidity. The average produced tracks is around 40 in p-Pb collisions, so the  $\eta$ -gap should not be too large, otherwise there are not enough tracks to get reliable results because the error bars will get too big. That is why there is an extra check for each event to be accepted, because each side has to have at least one track.

In this thesis there has been experimented with the  $\eta$ -gap. The most used values are 0 and 0.8. But for reference the values 0.2, 0.4, 0.6 and 1.0 are also evaluate in this thesis.

In figure 13 the  $v_2$  for these  $\eta$ -gaps are plotted as a function of  $p_T$ . The black markers represent the  $v_2$  with a  $|\Delta\eta| > 0.0$ . The green markers represent the  $v_2$  with a  $|\Delta\eta| > 0.2$ . The blue markers represent the  $v_2$  with a  $|\Delta\eta| > 0.4$ . The pink markers represent the  $v_2$  with a  $|\Delta\eta| > 0.6$ . The light blue markers represent the  $v_2$  with a  $|\Delta\eta| > 0.8$ . The red markers represent the  $v_2$  with a  $|\Delta\eta| > 1.0$ .

The expectation was that the  $v_2$  decreases with larges  $\eta$ -gap because the amount of non-flow removed increases. The results evaluated in this thesis confirm this.

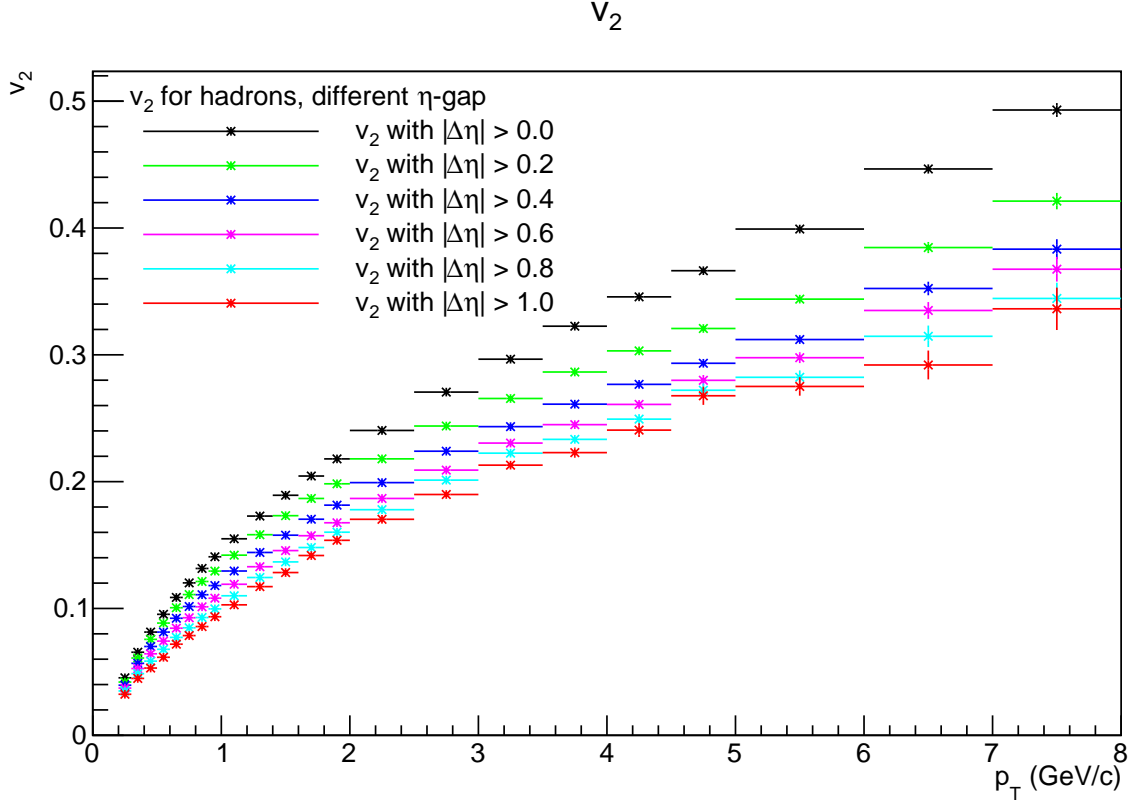


Figure 13:  $v_2$ -coefficient for (0-20%) multiplicity bin extracted using the Scalar Product with subevents for several  $\eta$ -gaps.

In figure 14 the difference in the method with and without subevents is plotted. The red circle markers represent the scalar product method without subevents, as explained in section 3.3 and the blue triangles markers represent the scalar product method with subevents. This plot is in the (0-20%) multiplicity bin for both methods and an  $\eta$ -gap of 0 is used.

The method with subevents has a much lower elliptic flow and is not as steep as the method without subevents. This is probably the result of the fact that tracks are only correlated with tracks from the opposite side of the TPC, instead of all tracks. Therefore tracks which are the result of a jet are not longer correlated with other tracks from the same jet. This removes non-flow correlation and this is visible in the results. Therefore the method with subevents is a good improvement in the Scalar Product and it will be used in this thesis for the next studies.

### 3.4 Non Uniform Acceptance-correction

The detector is supposed to be working correctly, but there could be some issues. For instance, if a read-out channel of the TPC is not working properly, an isotropic distribution can become anisotropic. To correct the results from this bias the NUA-correction (Non Uniform Acceptance-correction) is applied. Because all collisions and the direction of all final particles are randomly distributed, the  $\phi$  distribution should be flat. If this is not the case, the NUA-correction should be applied. This correction is explained and applied to charged particles.

The first check is to look at the  $\phi$  distribution. In figure 15 the  $\phi$  distribution of all charged particles is shown for the used dataset.

As seen from the figure, there is very little fluctuation, and the distribution is flat. Nevertheless, the NUA-correction is studied. The expectation is that the correction is not needed, because of the flat  $\phi$  distribution.

The formula for the NUA-correction is the following:

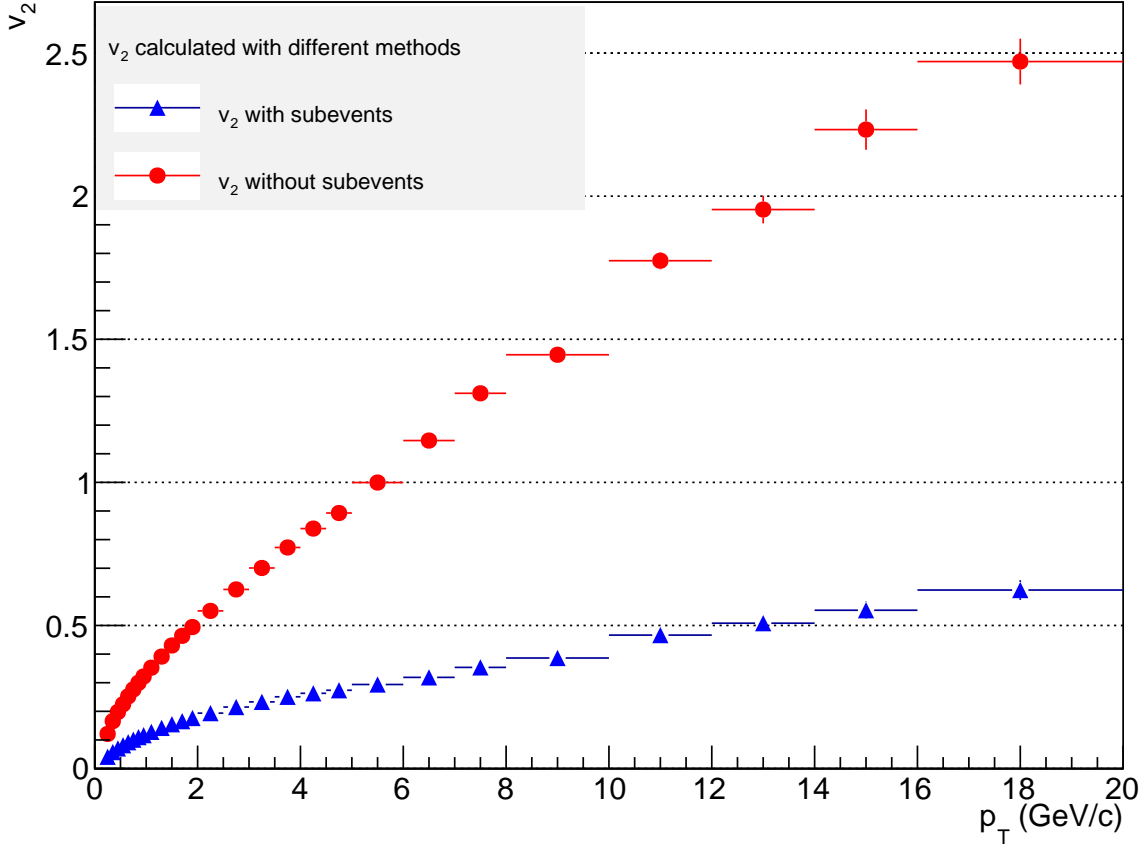


Figure 14:  $v_2$  calculated with the Scalar Product with subevents  $|\Delta\eta| > 0$  and without subevents in the (0-20%) multiplicity bin, shown in blue triangle and red circle markers respectively.

$$v_{2,corrected} = \frac{\langle\langle uQ^* \rangle\rangle/M - \langle\sin\phi_u\rangle\langle\sin\phi_Q\rangle - \langle\cos\phi_u\rangle\langle\cos\phi_Q\rangle}{\sqrt{\langle\frac{Q_a Q_b^*}{M_a M_b}\rangle - \langle Q_{a,x}\rangle\langle Q_{b,x}\rangle - \langle Q_{a,y}\rangle\langle Q_{b,y}\rangle}} \quad (16)$$

Where the  $\langle \rangle$  brackets stand for taking the mean over all events. The sine and cosine of the  $u$ -vector ( $\sin\phi_u$  and  $\cos\phi_u$ ) depends always on  $p_T$  but the mean sine and cosine of the  $Q$ -vector is  $p_T$  integrated, just like the terms in the denominator.  $\langle Q_{a,x} \rangle$  is the mean sine of all reference flow in the  $a$ -side, so  $\langle Q_{a,x} \rangle = \langle \sin\phi_Q \rangle_a$ . When the mean sine or cosine is calculated for the  $u$ -vector, the mean  $Q$ -vector comes from the other side, just like the  $\langle\langle uQ^* \rangle\rangle/M$  terms in the Scalar Product (equation 4). So in fact it is a bit more complicated. Note the extra labels in the following two equations:

$$v_{2,a,corrected} = \frac{\langle\langle uQ^* \rangle\rangle_a/M - \langle\sin\phi_u\rangle_a\langle Q_{b,x}\rangle - \langle\cos\phi_u\rangle_a\langle Q_{b,y}\rangle}{\sqrt{\langle\frac{Q_a Q_b^*}{M_a M_b}\rangle - \langle Q_{a,x}\rangle\langle Q_{b,x}\rangle - \langle Q_{a,y}\rangle\langle Q_{b,y}\rangle}} \quad (17)$$

$$v_{2,b,corrected} = \frac{\langle\langle uQ^* \rangle\rangle_b/M - \langle\sin\phi_u\rangle_b\langle Q_{a,x}\rangle - \langle\cos\phi_u\rangle_b\langle Q_{a,y}\rangle}{\sqrt{\langle\frac{Q_a Q_b^*}{M_a M_b}\rangle - \langle Q_{a,x}\rangle\langle Q_{b,x}\rangle - \langle Q_{a,y}\rangle\langle Q_{b,y}\rangle}} \quad (18)$$

Each side has to be corrected separately, because the  $a$ -side is different from the  $b$ -side. After the correction, the  $v_{2,a}$  and  $v_{2,b}$  have to be combined to give the final elliptic flow. The value and the size of the error bar is calculated is shown in the next equations. This is done for each  $p_T$ -bin separately.

$$v_{2,comb} = \frac{\frac{v_{2,a}}{\sigma_{v_{2,a}}^2} + \frac{v_{2,b}}{\sigma_{v_{2,b}}^2}}{\frac{1}{\sigma_{v_{2,a}}^2} + \frac{1}{\sigma_{v_{2,b}}^2}} \quad (19)$$

$$\sigma_{v_{2,comb}} = \frac{1}{\sqrt{\frac{1}{\sigma_{v_{2,a}}^2} + \frac{1}{\sigma_{v_{2,b}}^2}}} \quad (20)$$

Equation 17 and 18 have been applied to all charged particles, combined along the previous equations and the results are shown in figure 16. The  $v_2$  and corrected  $v_2$  are plotted in the same window, where the

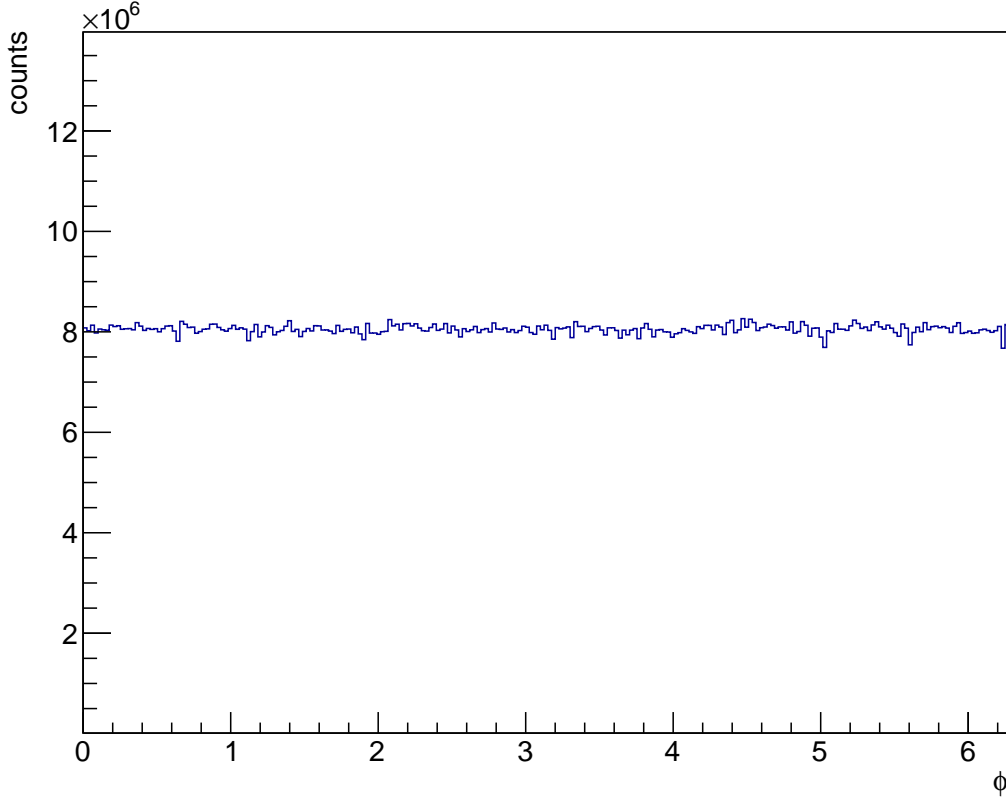


Figure 15:  $\phi$ -distribution of all tracks in all events analyzed.

black squared markers are the uncorrected  $v_2$  is and the red circle markers the corrected  $v_2$ . Because this gives not much insight, the ratio is also plotted in the right frame. Clear is that the ratio is very close to 1, and the correction does not influence the results. The error bars are the calculated by *ROOT*. Because the ratio is so close to 1, with a maximum discrepancy of 0.02%, there has been chosen to not include the NUA-correction in the final results.

### 3.5 Multiplicity bin subtraction

When the elliptic flow is calculated as explained in section 3.3.3, it also contains non-flow. For example there are tracks coming from jet fragmentation which have a correlation that has nothing to do with elliptic flow correlation. This aids to evaluate the global expansion of particles.

To remove the non-flow correlation, there is a subtraction done. How this is done, will be explained in this chapter. It is based on the *AA* – *pp*-method, explained by S. Voloshin [14]. *AA* and *pp* stand for heavy ion and proton-proton collisions respectively.

Both the numerator and the denominator from the scalar product formula (equation 4), can be decomposed as two different correlations. One is the interesting elliptic flow, and the other nonflow. The numerator becomes:

$$\langle u_i Q^* \rangle_{AA} = v_i v_Q M_{Q,AA} + \delta_{i,AA} M_{Q,AA} \quad (21)$$

where  $v_i$  and  $v_Q$  are the particle of interest (POI) and Q-vector flow,  $M_{Q,AA}$  the amount of particles used to build the Q-vector, also known as the multiplicity and  $\delta_{i,AA}$  is the average nonflow correlation between POIs and the Q-vector.

The denominator in equation 4 can be written as:

$$\langle Q_a Q_b^* \rangle_{AA} = v_Q^2 M_{Q,AA}^2 + \delta_{Q,AA} M_{Q,AA}^2 \quad (22)$$

where  $\delta_{Q,AA}$  is the nonflow correlation between  $Q_a$  and  $Q_b$ . Note that this is a different non-flow correlation variable as in equation 21. This is because the non-flow correlation between the particles of interest and Q-vector can be different from the non-flow correlation between the  $Q_a$  and  $Q_b$  vector.

Proton-proton collisions do not have any elliptic flow and thus any correlation is the result of non-flow. The scalar product equation for *pp* can be expressed in only one correlation:

$$\langle u_i Q^* \rangle_{pp} = \delta_{i,pp} M_{Q,pp} \quad (23)$$

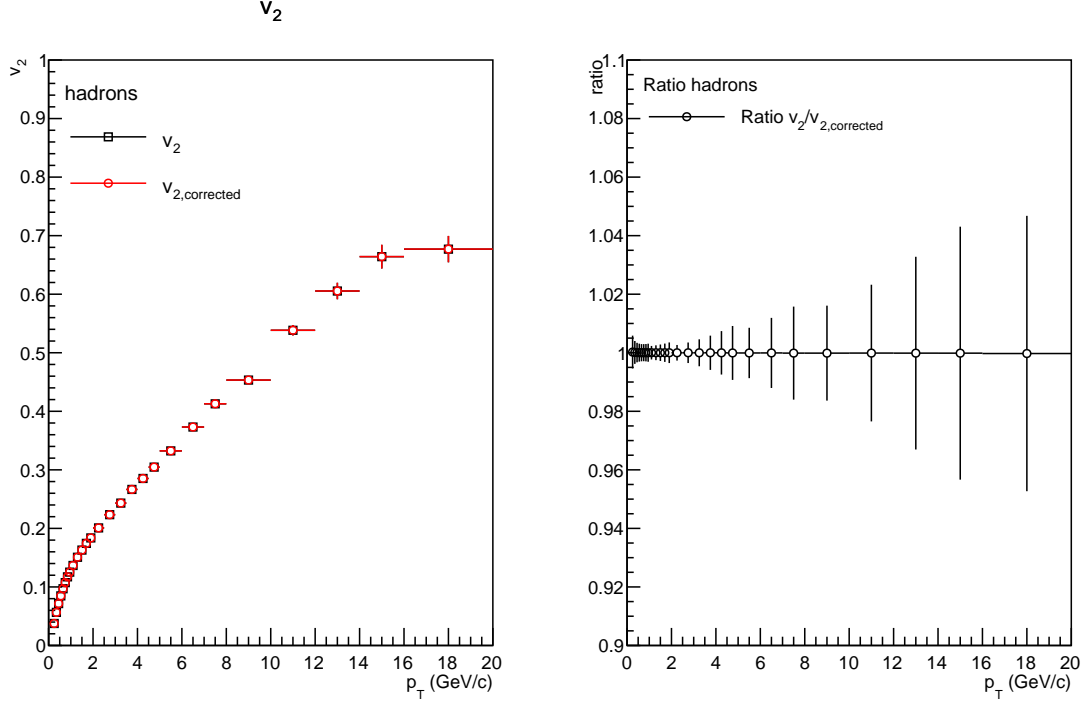


Figure 16: In the left panel the  $v_2$  and  $v_{2,corrected}$  for the NUA-correction are reported. In the right panel the ratio between the two is plotted.

And the denominator:

$$\langle Q_a Q_b^* \rangle_{pp} = \delta_{Q,pp} M_{Q,pp}^2 \quad (24)$$

The important assumption in this method is that the nonflow contribution for both collision systems is the same:

$$\delta_{AA} M_{Q,AA} = \delta_{pp} M_{Q,pp} \quad (25)$$

This must hold for the non-flow correlation  $\delta_i$  in the numerator, but as well for the non-flow correlation  $\delta_Q$  in the denominator.

If this assumption is true then equation 23 can be subtracted from equation 21 to give only the elliptic flow contribution in the  $AA$ -collision. The equations 24 and 22 cannot be done that easily because of the squared multiplicity. But when equation 24 first is multiplied by  $M_{Q,AA}$  and then divided by  $M_{Q,pp}$ , it can be subtracted. This gives the final equation in this method:

$$v_{2,AA-pp} = \frac{\langle uQ^* \rangle_{AA} - \langle uQ^* \rangle_{pp}}{\sqrt{\langle Q_a Q_b^* \rangle_{AA} - \langle Q_a Q_b^* \rangle_{pp} \frac{M_{Q,AA}}{M_{Q,pp}}}} \quad (26)$$

This method can be applied to proton-lead collisions, but using different multiplicity bins instead of different collision systems. The lowest multiplicity bins have the highest multiplicity, because the proton hits the lead ion in the middle, and interacts with more subatomic particles inside the ion. In this way, much more energy is transferred and converted to mass. In higher multiplicity bins, the proton hits the lead ion more peripheral, giving the proton less probability to transfer energy. When there are not enough interactions in such collisions, there could be smaller elliptic flow and mainly non-flow correlations. Under the assumptions that this nonflow correlation is the same in low and high multiplicity collisions, equation 28 can be used again. The  $AA$  in equation 28 becomes the lowest multiplicity, and  $pp$  the highest. The lowest multiplicity in this thesis is (0-20%) and the highest (60-100%). The assumptions that we make becomes:

$$\delta_{(0-20\%)} M_{Q,(0-20\%)} = \delta_{(60-100\%)} M_{Q,(60-100\%)} \quad (27)$$

The final equation that is used in this thesis is:

$$v_{2,((0-20\%)-(60-100\%))} = \frac{\langle uQ^* \rangle_{(0-20\%)} - \langle uQ^* \rangle_{(60-100\%)}}{\sqrt{\langle Q_a Q_b^* \rangle_{(0-20\%)} - \langle Q_a Q_b^* \rangle_{(60-100\%)} \frac{M_{Q,(0-20\%)}}{M_{Q,(60-100\%)}}} \quad (28)$$

### 3.5.1 Results

In figure 17 the elliptic flow results extracted using the Scalar Product method with  $|\Delta\eta| > 0$  is shown for different multiplicity bins. The red circle markers are the (0-20%) multiplicity bin, the green squared markers are the (20-40%) multiplicity bin, the blue triangles markers are the (40-60%) multiplicity bin and the black star markers are the (60-100%) multiplicity bin. There is seen that a lower multiplicity gives a higher calculated elliptic flow. This can be explained as following: most of these particles are created in a jet and have a huge correlation with other tracks from the same jet. This jet correlation could be stronger than the elliptic flow component in p-Pb collisions.

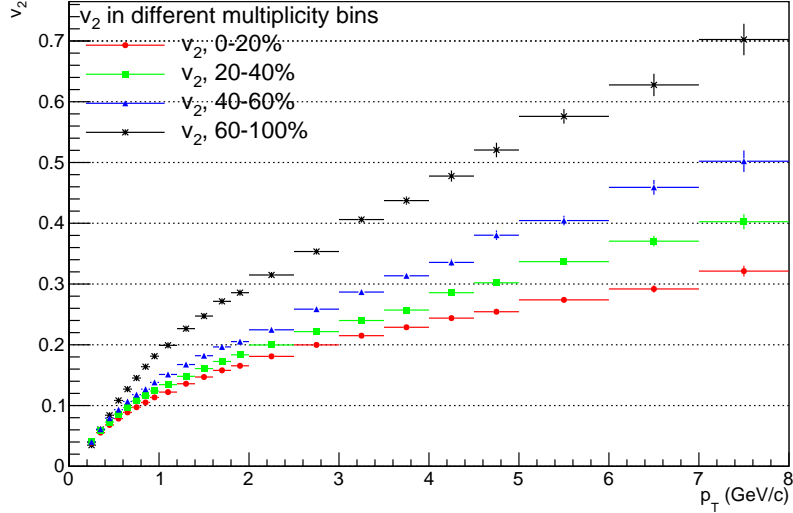


Figure 17:  $v_2$ -coefficient extracted using the Scalar Product with  $|\Delta\eta| > 0$  for the different multiplicity bins

In figure 18 the results of the subtraction are given for  $|\Delta\eta| > 0$ . In the left panel the results after subtraction are shown. In the middle panel the multiplicity bin (0 – 20%) is shown and in the right panel the highest centrality bin (60 – 100%). It is clear that the elliptic flow is a lot lower in the subtraction, and it decreases around  $p_T$  of 3 GeV/c.

The subtracted elliptic flow for all different  $\eta$ -gaps should be similar under the assumption that the  $\eta$ -gap will estimate the non-flow correlation in both multiplicity bins. In figure 19 the  $v_2$  is plotted for different  $\eta$ -gaps. The red full circle markers represent the  $v_2$  with  $|\Delta\eta| > 0.0$ . The green full squared markers represent the  $v_2$  with  $|\Delta\eta| > 0.2$ . The blue full triangle markers represent the  $v_2$  with  $|\Delta\eta| > 0.4$ . The pink open circle markers represent the  $v_2$  with  $|\Delta\eta| > 0.6$ . The teal open squared markers represent the  $v_2$  with  $|\Delta\eta| > 0.8$ . The black open triangle markers represents the  $v_2$  with  $|\Delta\eta| > 1.0$ .

In the low  $p_T$  range they differ because a different  $\eta$ -gap is applied results in a lower elliptic flow. It seems there are still effects such as mini-jets present which are supposed to be removed. However, the markers follow all the same trend and are roughly comparable within error bars. This was not the case before subtraction, previously shown in figure 13.

## 3.6 Particle Identification

In the second part of this thesis we study the Particle Identification in the ALICE detector. In lead-lead collisions there is a mass scaling and a proton crossover are observed, explained in section 1.2. These effects were also visible in proton-lead collisions when the  $v_2$ -coefficients are measured with the 2-particle correlation method. The next part will calculate the elliptic flow for different particle species, to see if these effects can be reproduced using the scalar product method.

The two used detectors for particle identification in this thesis are the Time Projection Chamber (TPC) and the Time Of Flight (TOF). The detector response is different for the different particle species. The particles that will be identified are pion, kaon and proton. There has been no distinction between particles and antiparticles. In the next paragraphs there will be explained why different particles have certain result, and how this is used for identification.

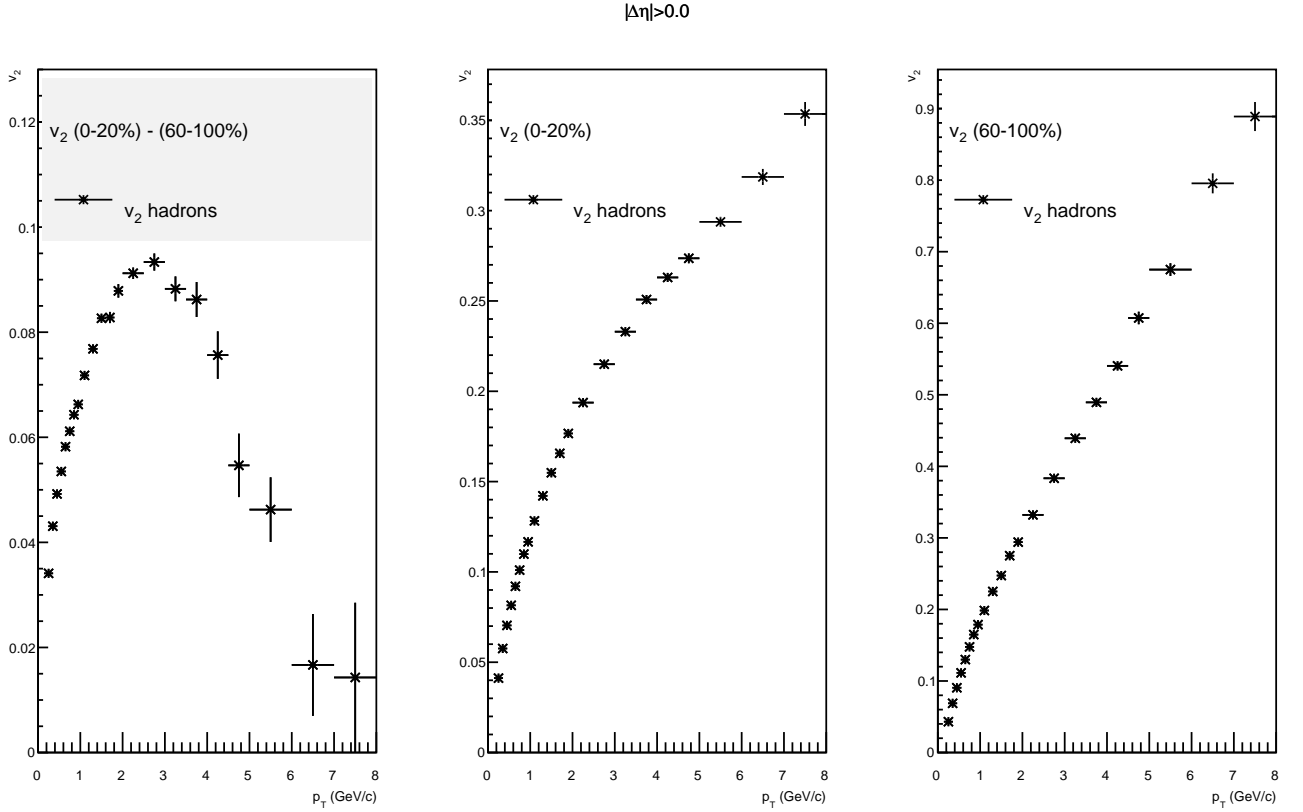


Figure 18: In the left panel the subtracted  $v_2$  coefficient is shown. In the middle and right panel the  $v_2$  coefficients are shown for the (0-20%) and (60-100%) multiplicity bin respectively, extracted using the Scalar Product, with  $|\Delta\eta| > 0$ . These two multiplicity bins are used for the subtraction.

### 3.6.1 PID using TPC

Each specie interacts differently with the drift gas within the TPC. This depends on many things, such as the velocity  $v$ , charge  $z$  and the atomic number ( $Z$ ), amount of electrons per  $\text{cm}^3$  ( $n$ ) and excitation potential ( $I$ ) of the gas. The gas consist of 85%  $\text{Ne}_2$ , 10%  $\text{CO}_2$  and 5%  $\text{N}_2$ . The Bethe formula can calculate the energy loss:

$$-\frac{dE}{dx} = \frac{4\pi n z^2 Z^2 e^4}{m_e v^2} \left[ \ln\left(\frac{2m_e v^2}{I(1-\beta^2)}\right) - \beta^2 \right] \quad (29)$$

This is negative because there is a loss of energy per distance travelled. The amount is different for each particle, but it depends hugely on the momentum. In figure 21 the  $dE/dx$  for all accepted tracks is plotted against the momentum. In the low  $p$  range there are several lines distinguishable. Upon zooming on the  $0 < p < 2$  range, there are different lines visible.

The horizontal line between 40 and 60 MeV/cm are pions. The horizontal line between 70 and 100 MeV/cm represent electrons. The curved band starting in the picture at 500 MeV/c are kaons, and the band starting at 0.7 GeV/c are protons. There is also a band with relative very few particles, those are likely heavy particles, such as deuterium or tritium. There are relatively too few of them to do more research in it.

These lines or bands are universal in the Time Projection Chamber, when the same condition apply, such as the gas mixture. The lines are calculated and are gaussians on the  $(p, dE/dx)$ -diagram. The closer a track with a certain momentum and energy loss is to such a line, the likelier it is to be that associated specie. This probability is expressed in sigma's from the previously mentioned gaussians. To distinguish between lower and higher then expected values, the sigma's can also be negative:

$$\sigma_{TPC} = \frac{dE}{dx} \Big|_{calc} - \frac{dE}{dx} \Big|_{exp} \quad (30)$$

Because there is quite a big overlap for a  $p > 1$  GeV/c, the signal from the Time Of Flight detector is also used. This is discussed in the next paragraph.

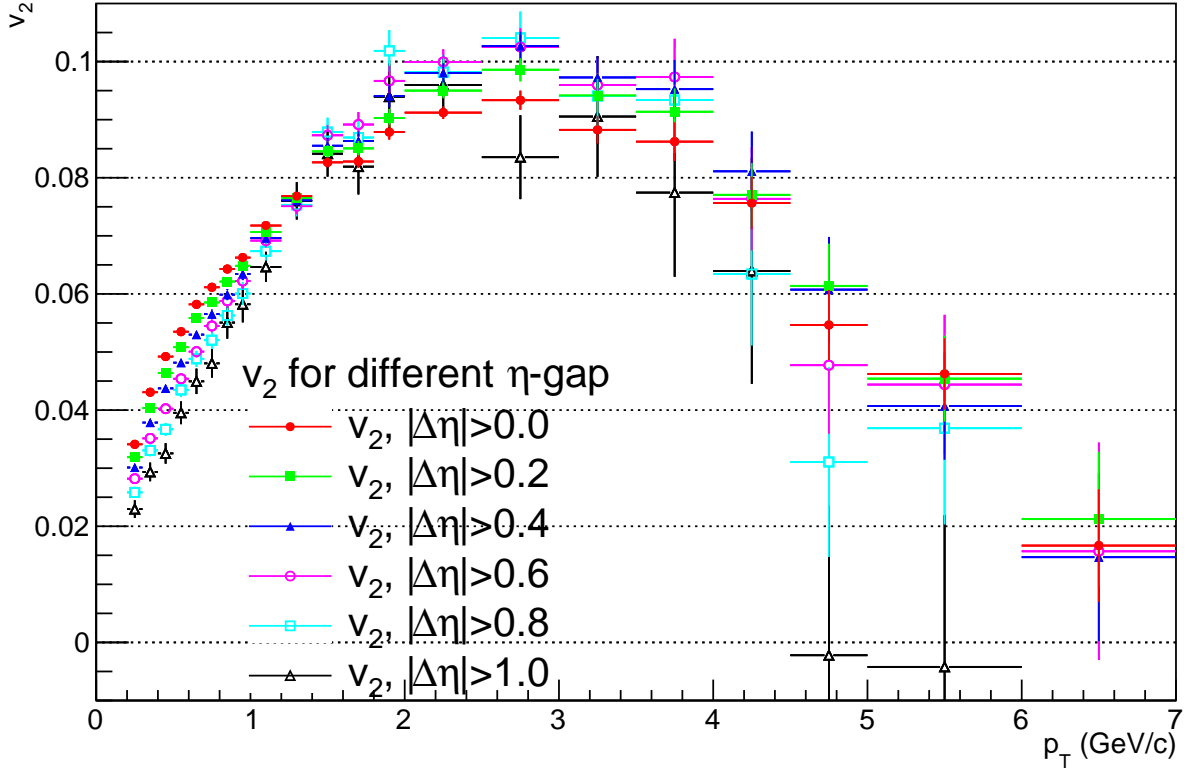


Figure 19:  $v_2$ -coefficients after subtraction for different  $\eta$ -gaps.

### 3.6.2 PID using TOF

There is another directly observable helps in particle identification, which is the time of flight. This differs because the mass is different for possible particles. How the mass effects the time of flight, is explained in the next section.

The velocity  $v$  normalised to the speed of light  $c$  is equal to  $\frac{p}{E}$  in natural units, which is equal to:

$$\frac{v}{c} = \beta = \frac{p}{E} = \frac{p}{\sqrt{p^2 + m^2}} \quad (31)$$

The time  $T$  a particle has to travel depends on the distance travelled from the detector  $L$ . Fill in  $\beta$  from equation 31:

$$T = \frac{L}{v} = \frac{L}{\beta c} = \frac{L\sqrt{p^2 + m^2}}{pc} \quad (32)$$

This gives an expected time, depending on momentum, for each different particle. Because a proton is around 10 times heavier than a pion, it would require more time for a proton to reach the detector. When the momentum is higher, the influence of the mass becomes smaller and the expected travel time for different particles are closer to each other. Because the expected time depends on the traveled distance, the  $\beta$  is plotted against the momentum, instead of  $T$ . This conversion does not nullify the expectation because of the connection between  $T$ ,  $L$  and  $\beta$ , shown in equation 32.

The results for the  $\beta$  of all accepted hadrons is shown in figure 22. Just like with the  $dE/dx$  for all hadrons, there are multiple bands visible. They may be not very distinctive, but the yellow area is around a thousand times more dense than the light blue area. The lightest particles have the highest velocity. From high  $\beta$  to low, the particles are pions, kaons and protons. In figure 23 there has been zoomed in in the low  $p$ -range to have a better look at the differences. After  $p_T \sim 2.5$  GeV/c the bands of the different species are cluttered together.

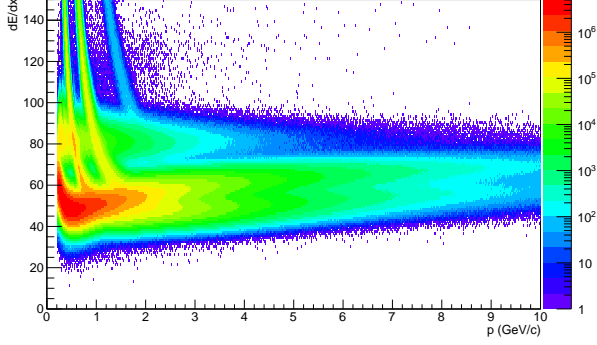


Figure 20:  $dE/dx$  for all charged particles.

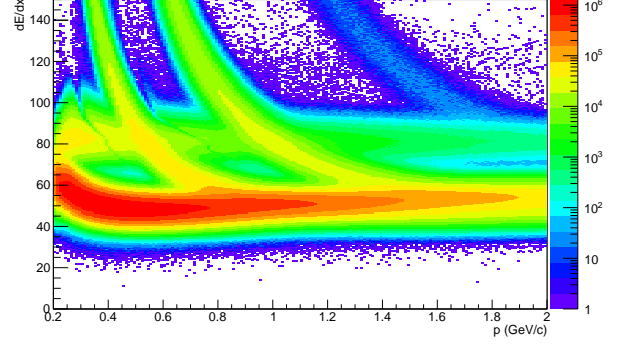


Figure 21:  $dE/dx$  for all charged particles, zoomed.

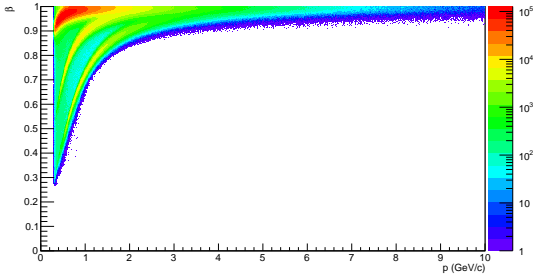


Figure 22:  $\beta$  for all charged hadrons.

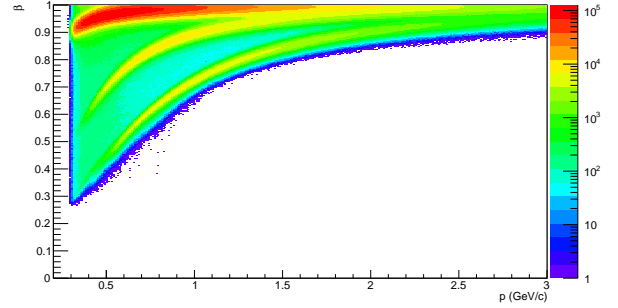


Figure 23:  $\beta$  for all charged hadrons, zoomed.

### 3.6.3 Combining and selecting

Now that the sigma's for different particles are defined from the TPC and TOF detectors, they can be combined in order to have better particle identification. That is done with the following formula:

$$\sigma_{total} = \sqrt{\sigma_{TPC}^2 + \sigma_{TOF}^2} \quad (33)$$

where  $\sigma_{TPC}$  and  $\sigma_{TOF}$  are the number of sigma's for the TPC and TOF respectively and this is done for all particles independently. The total sigma ( $\sigma_{total}$ ) is finally used to distinguish the different species.

If  $\sigma_{total}$  is lower than 3 for just one particle, the track is assigned to be that particle. There is no need to take the absolute value, because if there were any negative sigma's, they would have canceled out because of the square. When there are more possible identifications, that means there are more  $\sigma_{total} < 3$ , the track is rejected, for example if both  $\sigma_{total}^p > 3$  and  $\sigma_{total}^\pi > 3$ . This can happen when the different species bands are close to each other in TPC and TOF. The track is still used for the Q-vector since its built using all charged particles, but not for particle identification. This is done to keep the contamination as low as possible. The downside of this approach is that it removes lots of potential good particles and has as effect that there is less particle data available at high  $p_T$ -range ( $> 3$  GeV/c) which is reflected in bigger error bars. At lower  $p_T$  there is no overlap in the  $dE/dx$  or  $\beta$  plots, so the particle identification works very well there. At higher  $p_T$  the overlap increases which makes the particle identification less precise.

### 3.6.4 Results PID

The final  $dE/dx$  and  $\beta$ -plots using equation 33 are shown in figures 24 through 29 as a function of  $p_T$ . The previous mentioned particle bands are visible for both  $dE/dx$  as  $\beta$ . There are less identifications at higher  $p_T$  because the bands are overlapping. A way to improve this is with more drastic cuts, but this is not done for this thesis.

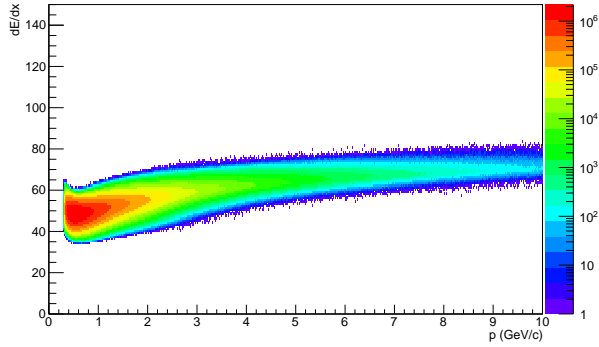


Figure 24:  $dE/dx$  of all pions

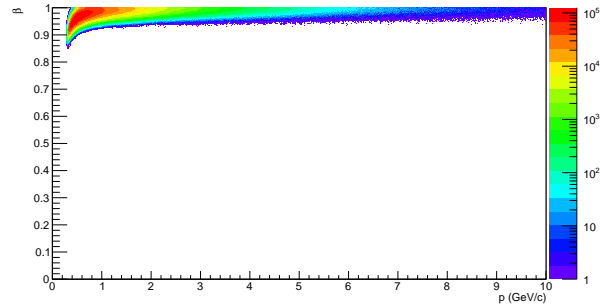


Figure 25:  $\beta$  of all pions

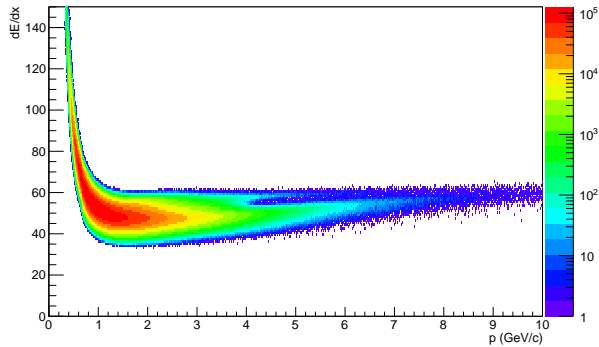


Figure 26:  $dE/dx$  of all kaons

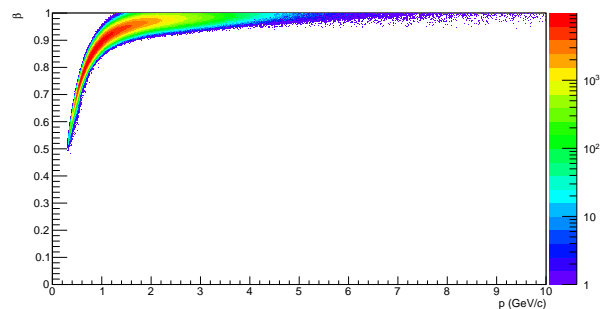


Figure 27:  $\beta$  of all kaons

### 3.6.5 Further checks on PID at high $p_T$

In order to study in detail the performance of the detectors used in order to see if the particle identification can be improved at high  $p_T$ , we also employed a different PID strategy in this region. One thing was to not use the signal from the TOF-detector for particle identification. At high  $p_T$  the tracks are relativistic and the time of flight is not a good way to distinguish different species. This leaves only the signal from the TPC. Because the  $dE/dx$  is so much overlapping as seen in figure 21, the former sigma limit of 3 is not acceptable. Instead of that there are two new limits tried:  $|\sigma_{TPC}| < 2$  and  $|\sigma_{TPC}| < 1.5$ . Also multiple identifications are treated differently. Instead of removing the tracks, it is assigned to the particle species with the lowest sigma. The crossover between using both detectors and only TPC, is at  $p_T = 4$  GeV/c. The result of these corrections are shown in figures 30 through 35.

From this figures is clear that the transition is never smooth. For example, in figure 30 there are suddenly more pion identifications. It is even worse in figure 31. There are not only more identification, but also in a different  $dE/dx$  region. This was the reason to lower the sigma threshold to 1.5.

With this new limit, there is still not a smooth crossover. In the kaon and proton figures (figure 34 and 35) there are still suddenly much more particle identification after the crossover. The pions are looking better, but the other two particle species are not showing much progress. Because lack of time, further investigation was not done in this thesis. The reason was that the TOF signal was not very distinctive at high  $p_T$ , but TOF and TPC signals combined is probably better then only TPC. Therefore, all the results will be using the particle identification used in equation 33, with a threshold of  $\sigma_{total} < 3$ . For further studies different PID strategy at high  $p_T$  will be investigated. For example, in figure 36 the purity of proton as a function of  $p_T$  is shown. The purity increases to 0.9 from 0.7 for high  $p_T$  range, with a stronger cut on the TOF.

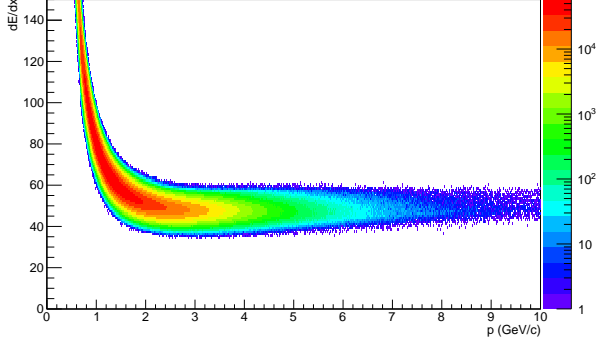


Figure 28:  $dE/dx$  of all protons

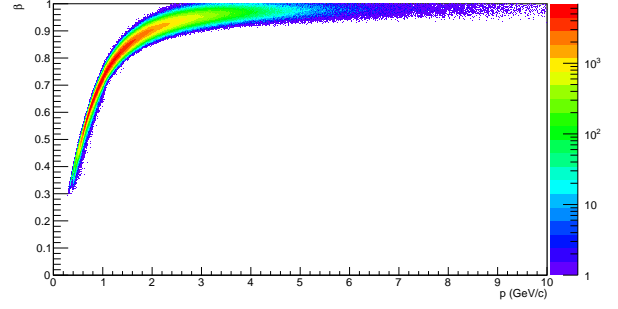


Figure 29:  $\beta$  of all protons

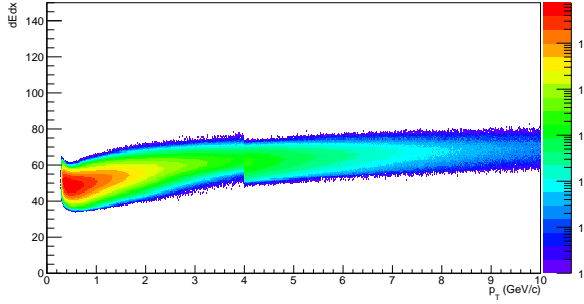


Figure 30: Pion,  $|\sigma_{TPC}^\pi| < 2$

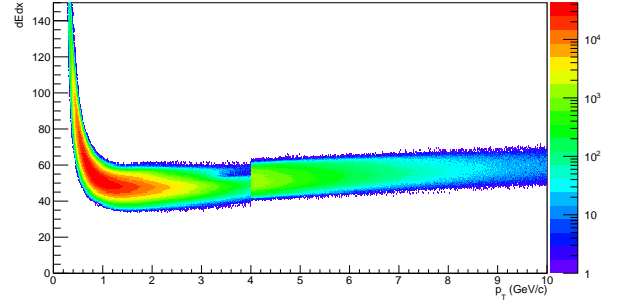


Figure 31: Kaon,  $|\sigma_{TPC}^K| < 2$

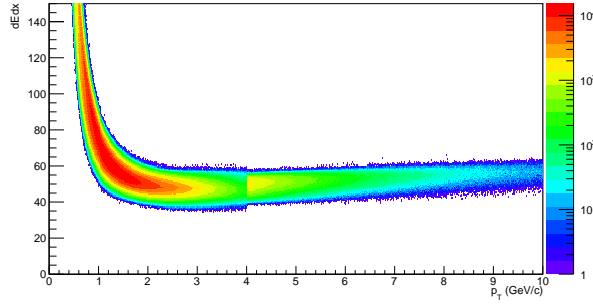


Figure 32: Proton,  $|\sigma_{TPC}^p| < 2$

### 3.6.6 NUA-correction for particles

The NUA-correction for each distinctive particle is also interesting and should be verified if the correction is needed or not. Just as with the hadrons, explained in section 3.4, the first check is see if the  $\phi$ -distribution is as flat as the one from charged particles. The figures are shown in 37, 38 and 39 for pions, protons and kaons respectively. Also the  $\phi$ -distribution for charged particles is shown for comparison in figure 40. It is easily seen that all distributions are not flat, and the NUA-correction should have a bigger impact on the particles species then it had on the charged particles.

But first there is a little change in the calculation. The particles of interest are only the tracks that are identified as a certain specie. That is the only change, the reference flow stays the same and also the combining technique is used from equations 19 and 20.

Thus these following equations are used for the NUA-correction for particles. The superscript  $p$  denotes that it is coming from a proton. It can be exchanged for a  $\pi$  or K, for the correction for pions or kaons, respectively.

$$v_{2,a,corrected}^p = \frac{\langle uQ^* \rangle_a^p - \langle \sin \phi_u \rangle_a^p \langle Q_{b,x} \rangle - \langle \cos \phi_u \rangle_a^p \langle Q_{b,y} \rangle}{\sqrt{Q_A Q_B^* - \langle Q_{a,x} \rangle \langle Q_{b,x} \rangle - \langle Q_{a,y} \rangle \langle Q_{b,y} \rangle}} \quad (34)$$

$$v_{2,b,corrected}^p = \frac{\langle uQ^* \rangle_b^p - \langle \sin \phi_u \rangle_b^p \langle Q_{a,x} \rangle - \langle \cos \phi_u \rangle_b^p \langle Q_{a,y} \rangle}{\sqrt{Q_A Q_B^* - \langle Q_{a,x} \rangle \langle Q_{b,x} \rangle - \langle Q_{a,y} \rangle \langle Q_{b,y} \rangle}} \quad (35)$$

The results are shown in pictures 41, 42 and 43 for pions, protons and kaons respectively. This is done an

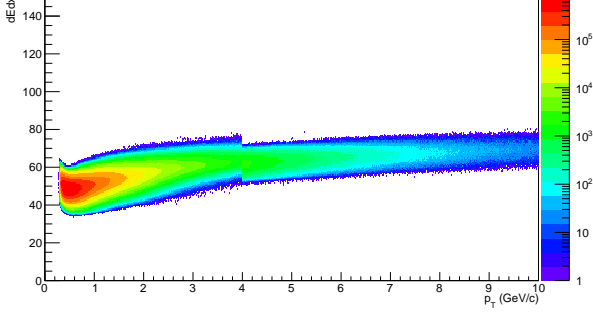


Figure 33: Pion,  $|\sigma_{TPC}^{\pi}| < 1.5$

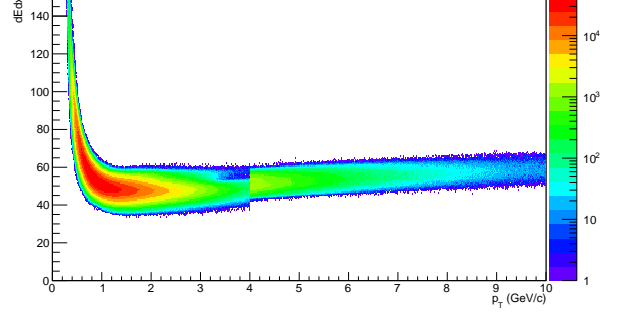


Figure 34: Kaon,  $|\sigma_{TPC}^K| < 1.5$

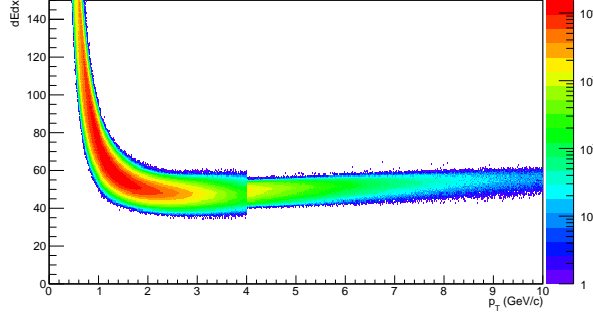


Figure 35: Proton,  $|\sigma_{TPC}^p| < 1.5$

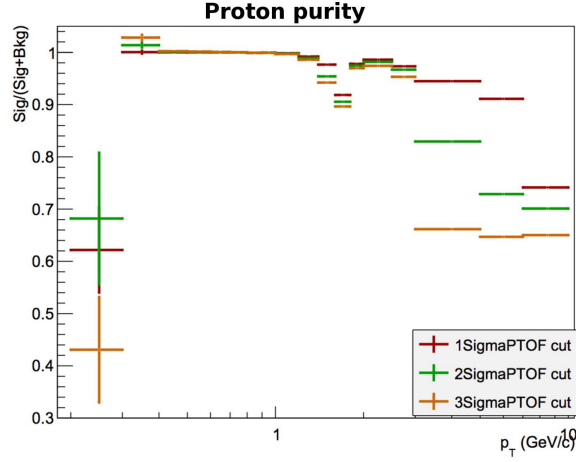


Figure 36: Purity of proton [15]

$\eta$ -gap of 0, in all multiplicity bins and without subtraction. The same layout as for the charged particles is chosen. That means that in the left panel the normal  $v_2$  and the  $v_{2,corrected}$  are shown on top of each other, and in the right panel the ratio between these two. The only difference is the  $p_T$  range. Because particle identification is not completely reliable after  $p_T = 4$  GeV/c, this is the maximum  $p_T$  that is shown in this thesis. Even with the rather bumpy distribution, the ratio is still very close to 1. The largest deviation is in the low  $p_T$  range, but is for all particles lower than 2%. The points that are very defective are the cause of too few data available in that particular bin. Therefore the  $v_2$  and the correction look unlikely, but this is ok.

After  $p_T = 1$  GeV/c the difference is lower than 0.1%. The reason for this is that the distribution for the reference flow is still flat. This makes the correction terms in the numerator of equations 34 and 35 neglectable in comparison. The correction in the denominator of the same equation is the same as for the charged particles. The correction terms  $\langle Q_{a,x} \rangle \langle Q_{b,x} \rangle - \langle Q_{a,y} \rangle \langle Q_{b,y} \rangle$  are a factor  $10^5$  smaller than the normal  $\sqrt{Q_A Q_B^*}$ , so that does not change anything too.

Because the correction is below 1% for all species, the NUA-correction is also not applied to different species in the final results.

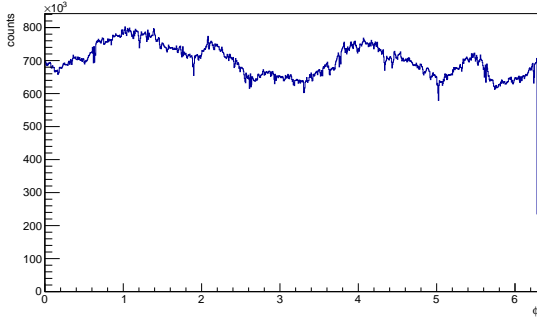


Figure 37:  $\phi$ -distribution of all pions

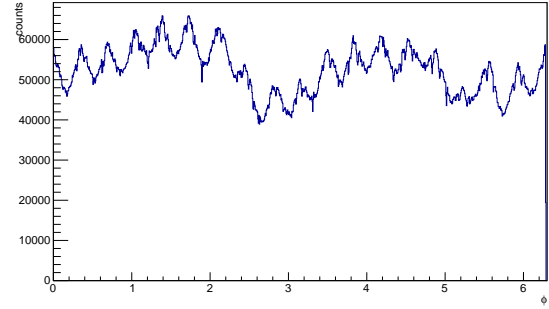


Figure 38:  $\phi$ -distribution of all protons

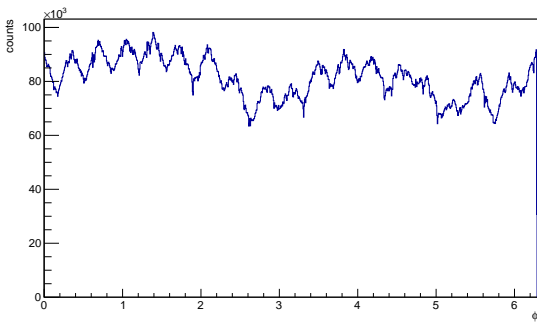


Figure 39:  $\phi$ -distribution of all kaons

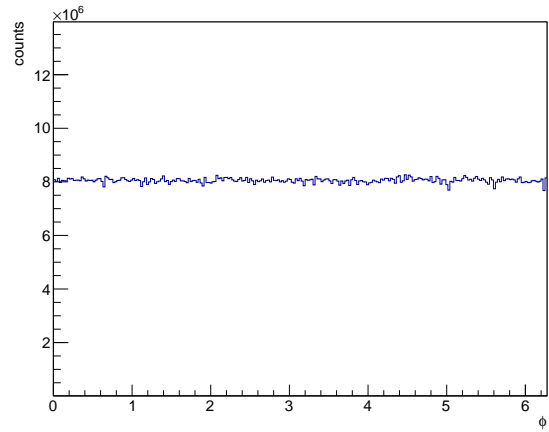


Figure 40:  $\phi$ -distribution of all charged particles

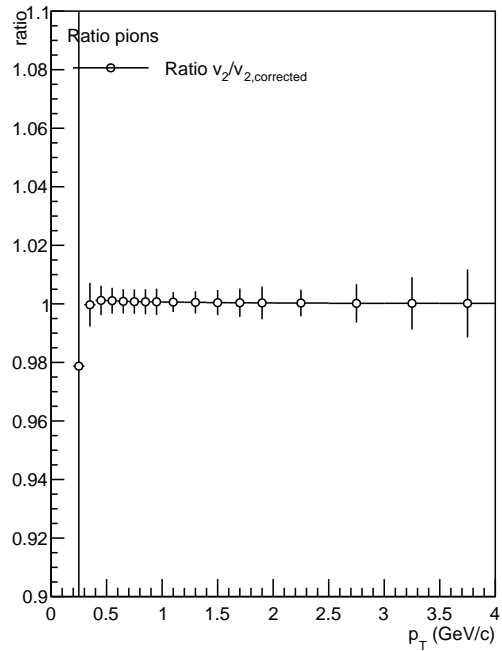
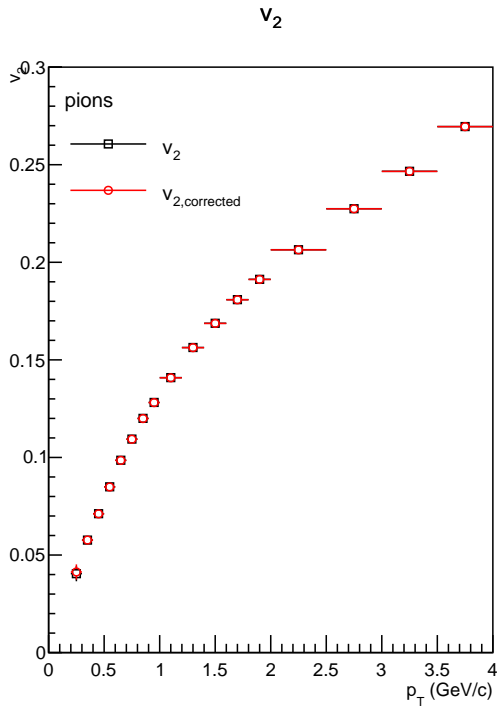


Figure 41: In the left panel the  $v_2^\pi$  and  $v_{2,corrected}^\pi$  for the NUA-correction are reported. In the right panel the ratio between the two is plotted.

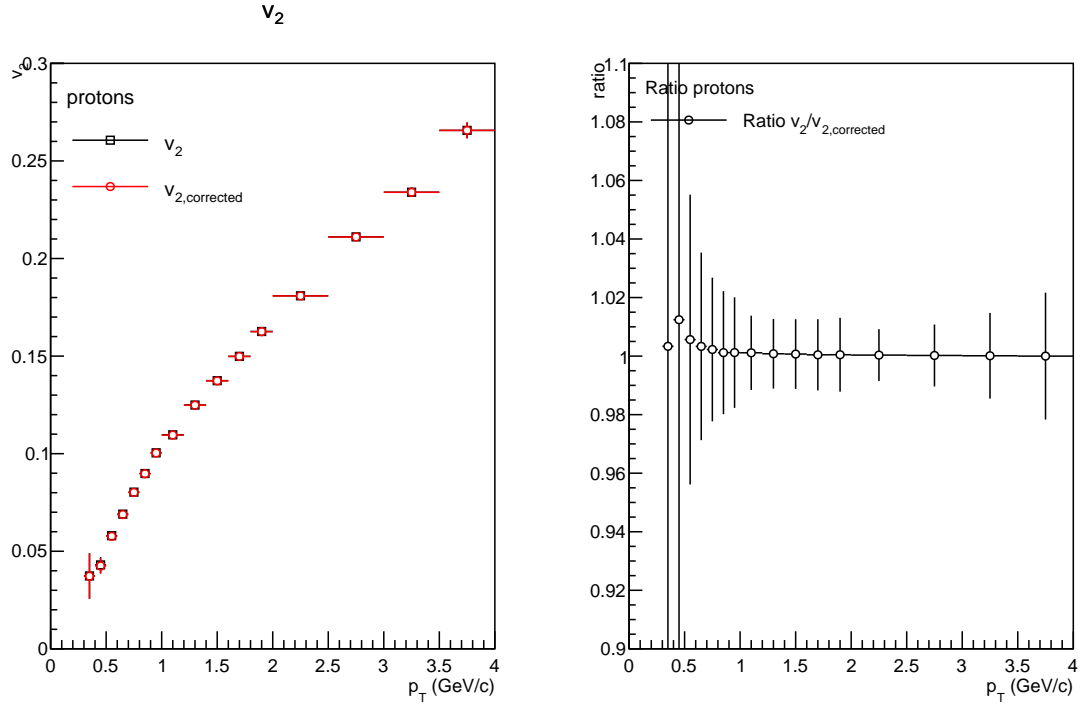


Figure 42: In the left panel the  $v_2^p$  and  $v_{2,corrected}^p$  for the NUA-correction are reported. In the right panel the ratio between the two is plotted.

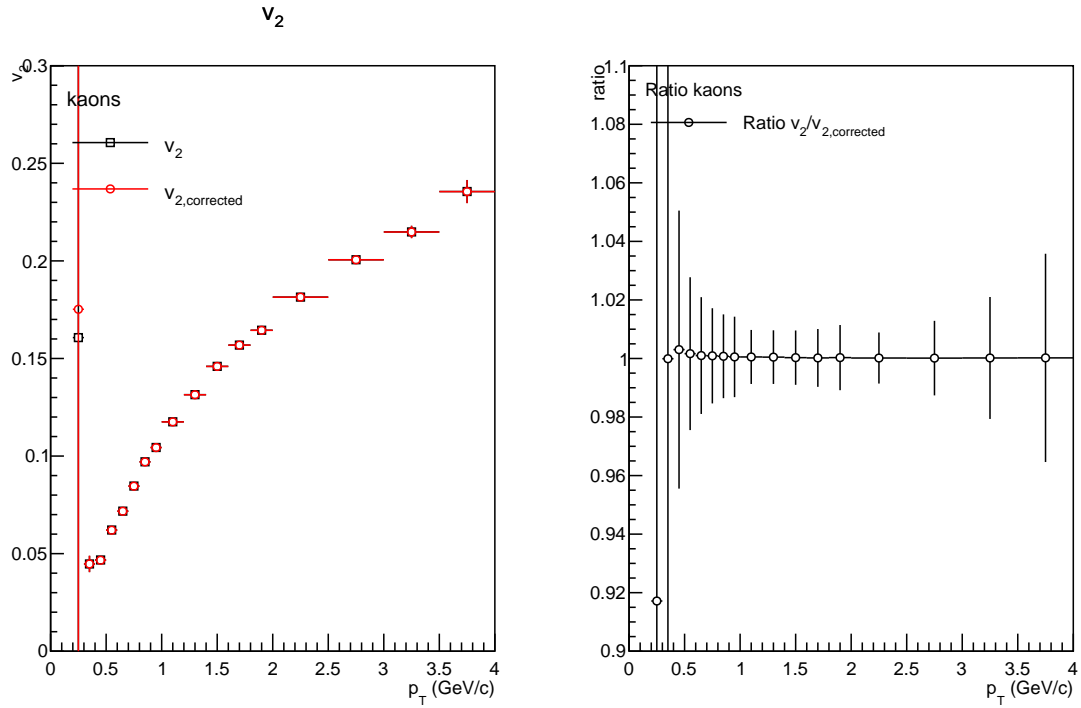


Figure 43: In the left panel the  $v_2^K$  and  $v_{2,corrected}^K$  for the NUA-correction are reported. In the right panel the ratio between the two is plotted.

### 3.6.7 Subtraction for particles species

The next step is doing the subtraction for pion, proton and kaon respectively. This follows the same idea explained in section 3.5. The final equation is the following:

$$v_{2,((0-20\%)-(60-100\%))} = \frac{\langle uQ^* \rangle_{(0-20\%)} - \langle uQ^* \rangle_{(60-100\%)}}{\sqrt{\langle Q_a Q_b^* \rangle_{(0-20\%)} - \langle Q_a Q_b^* \rangle_{(60-100\%)}} \frac{M_{Q,(0-20\%)}}{M_{Q,(60-100\%)}}} \quad (36)$$

From here, it is just a few steps to the subtraction for particles. The denominator is completely the same, because the reference flow (Q-vector) is the same for charged particles as for the different species. The numerator however, is slightly different. The flow from the particles of interest is restricted to only identified particles. For example, if the flow for protons is needed to be calculated, only identified protons act as particles of interest  $u$ . That is the same for both multiplicity bins. For clarity, an extra index can be added, like is done in the following formula:

$$v_{2,((0-20\%)-(60-100\%))}^p = \frac{\langle uQ^* \rangle_{(0-20\%)}^p - \langle uQ^* \rangle_{(60-100\%)}^p}{\sqrt{\langle Q_a Q_b^* \rangle_{(0-20\%)} - \langle Q_a Q_b^* \rangle_{(60-100\%)}} \frac{M_{Q,(0-20\%)}}{M_{Q,(60-100\%)}}} \quad (37)$$

where  $v_2^p$  is the elliptic flow of protons in this case. This can be done for all three particles: proton, pion and kaon. This is the only difference between subtraction for hadrons and distinctive particles.

### 3.6.8 Results subtraction PID

The results of the subtraction for different particle species are reported in figures 44 through 49 for all different  $\eta$ -gaps. In all figures the black circle markers represent the hadrons, the green square markers represent the pions, the blue triangle markers represent the protons and the pink cross markers represent the kaons. In all figures we can see the mass-scaling and the proton crossover, which were also observed in Pb-Pb and p-Pb collisions when the 2 Particle Correlation was used.

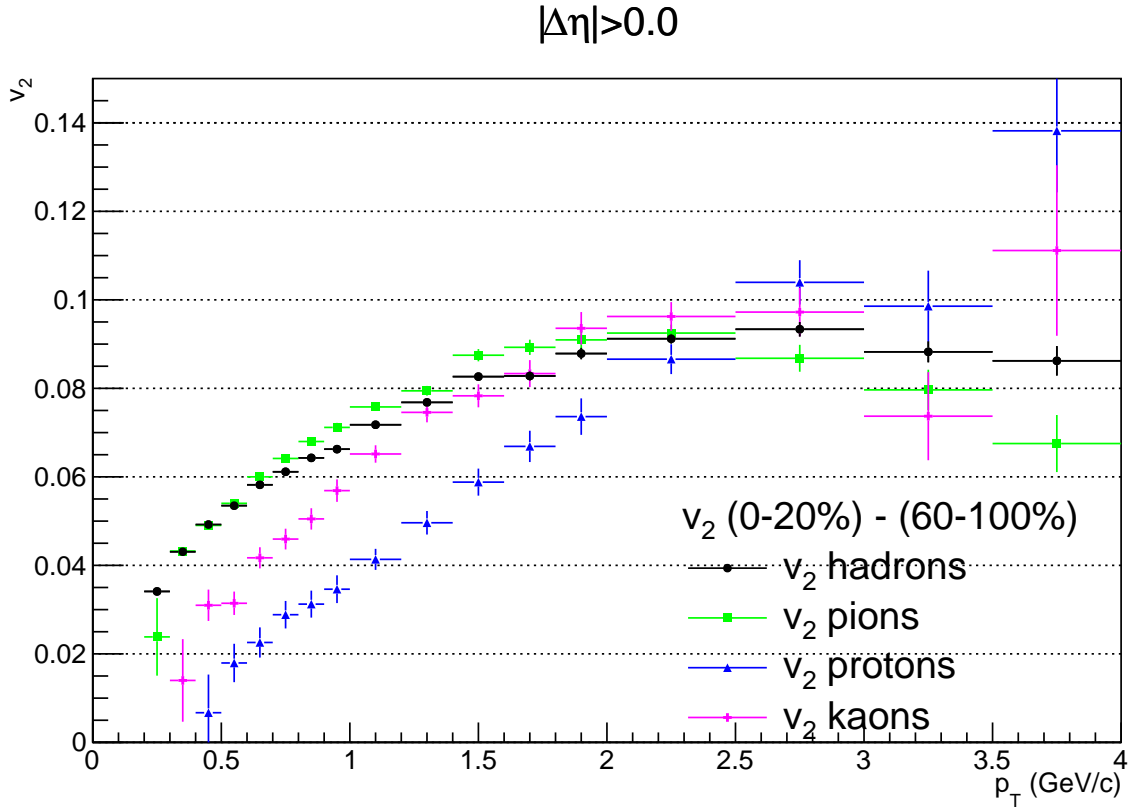
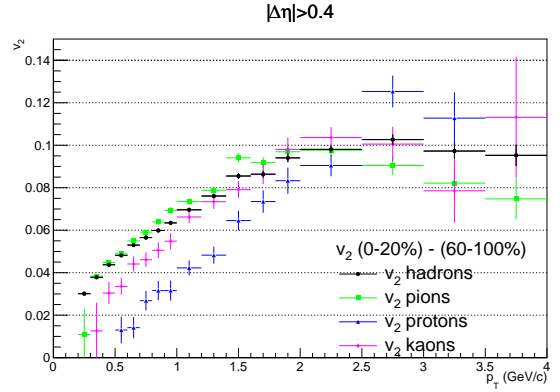
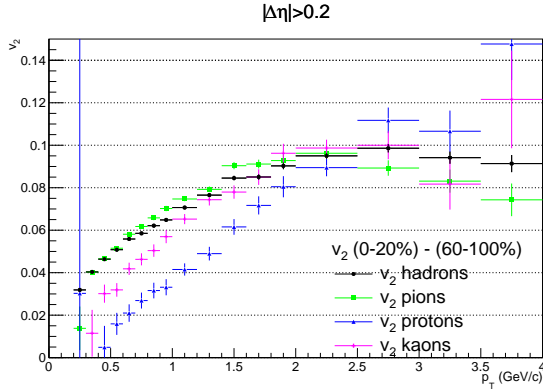
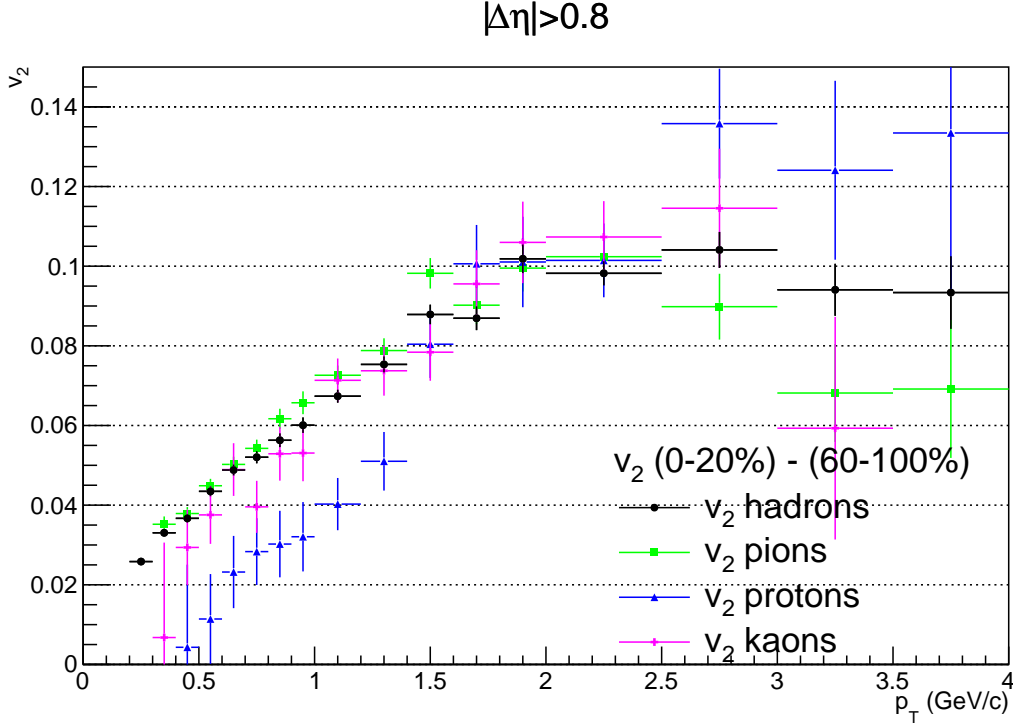


Figure 44: Final  $v_2$  result,  $|\Delta\eta| > 0.0$



## 4 Conclusion

The main goal of this thesis was to extract the  $v_2$ -coefficients from p-Pb collisions using the Scalar Product method. To remove as much non-flow correlations as possible, such as jet fragmentation, two subevents with different  $\eta$ -gap are used to deliver the  $u$ -vector and  $Q$ -vector. To correct for any non-uniformity acceptance in the detector the NUA-correction had been studied but we observed that this correction was not important, due to the flat  $\phi$ -distribution for charged particles in the ALICE detector. A subtraction had been done between the (0-20%) and (60-100%) multiplicity bins to remove non-flow effects under the assumptions that the non-flow is the same in different multiplicity bins.

Particle identification was an important part of this thesis because the mass-scaling at low  $p_T$  and proton crossover effects were both visible in Pb-Pb and p-Pb collisions according to previous measurements [4][5]. In this thesis the PID is done using signals from the TPC and TOF detectors. The NUA-correction was also applied for different particle species. Just like charged particles, it was found that the correction was not important. After the subtraction the mass scaling and proton crossover were visible in the results, for all different applied  $\eta$ -gaps. This means it can be a good hint to continue investigate the existence of a Quark-Gluon Plasma through the collective phenomena and improve the technique to study non-flow contributions in p-Pb collisions.

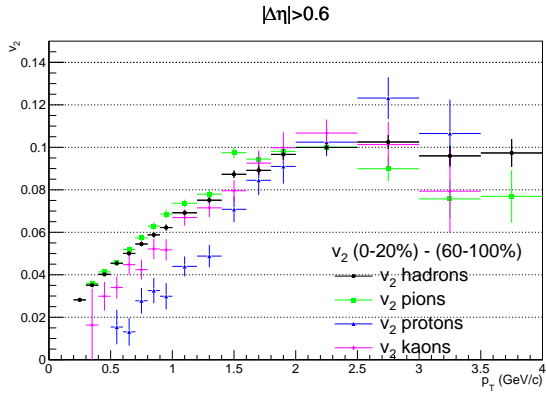


Figure 48: Final  $v_2$  result,  $|\Delta\eta| > 0.6$

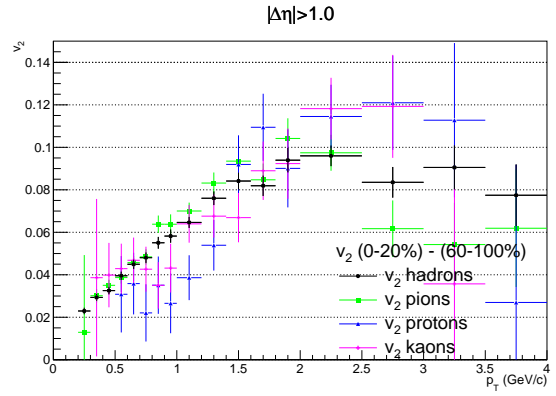


Figure 49: Final  $v_2$  result,  $|\Delta\eta| > 1.0$

## References

- [1] ALICE Collaboration *ALICE: Physics Performance Report, Volume I* CERN, Geneva, Switzerland, 19 october 2004
- [2] R. Snellings, [arXiv:1102.3010v2 [nucl-ex]].
- [3] The ALICE collaboration *Elliptic Flow of Charged Particles in Pb-Pb Collisions at  $\sqrt{S_{NN}} = 2.76$  TeV*
- [4] The ALICE collaboration, [arXiv:1205.5761v2 [nucl-ex]]
- [5] The ALICE collaboration, [arXiv:1307.3237v3 nucl-ex]]
- [6] L. Milano, [arXiv:1308.3623v1 [hep-ex]]
- [7] <http://aliceinfo.cern.ch/TPC/node/7>
- [8] [http://aliceinfo.cern.ch/secure/system/files/documents/run\\_coordination/Run-2009-2010/ALICE\\_coordinates.png](http://aliceinfo.cern.ch/secure/system/files/documents/run_coordination/Run-2009-2010/ALICE_coordinates.png)
- [9] <http://www.quantumdiaries.org/wp-content/uploads/2010/04/TPCPic.lowres1.png>
- [10] A. Akindinov et al., *The multigap resistive plate chamber as a time-of-flight detector*, <http://citeseerx.ist.psu.edu/viewdoc/download?doi=10.1.1.205.7315&rep=rep1&type=pdf>
- [11] [http://aliceinfo.cern.ch/Public/en/Chapter2/Chap2\\_TOF.html](http://aliceinfo.cern.ch/Public/en/Chapter2/Chap2_TOF.html)
- [12] The ALICE collaboration, *ALI-PERF-51411*
- [13] ALICE Collaboration, [arXiv:1307.3237v2 [nucl-ex]]
- [14] S. A. Voloshin, *Flow notebook*, 25 february 2013. Internal document
- [15] R.E. De Boer,  *$K_S^0$ -p correlations in p-Pb collisions at  $\sqrt{S_{NN}} = 5.02$  TeV/c*, draft 5<sup>th</sup> January 2014

## List of Figures

1	The overlapping volume in a non-central heavy ion collision [2] . . . . .	4
2	Difference between the Reaction plane and the Participant plane [2] . . . . .	4
3	Results of the ALICE collaboration on the elliptic flow measurements in Pb-Pb collisions for charged particles only [3]. In the upper panel the difference between the $v_2\{2\}$ and $v_2\{4\}$ is shown. The $v_2\{2\}$ is shown in blue star markers, and the $v_2\{4\}$ in red triangles. In the lower panel the results of $v_2\{4\}$ in different centrality bins is shown in comparison to RHIC experiments. The blue circle markers represent the (10-20%) centrality bin, in red squared markers the (20-30%) bin and the green triangle markers the (30-40%) bin. . . . .	5
4	Results of the ALICE collaboration on the elliptic flow measurements in Pb-Pb collisions for different species [4]. The red, blue and green markers represent the pion, proton and kaon respectively. . . . .	6
5	Results of the ALICE collaboration on the elliptic flow calculation in p-Pb collisions [5]. The black square, red triangle, blue circle and green star markers represent the charged particles, pion, proton and kaon respectively. . . . .	6
6	Overview of the ALICE detector with multiple detectors labeled. [8] . . . . .	7
7	Overview of the ITS detector in ALICE [1] . . . . .	7
8	A single strip of the ALICE TOF detector [1] . . . . .	8
9	Working principle of the TOF-detector [11] . . . . .	8
10	Correlation between centrality determination and multiplicity. In the left panel this correlation is shown for p-Pb collisions, in the right panel for Pb-Pb collisions. [12] . . . . .	9

11	Multiplicity distribution for different multiplicity bins . . . . .	9
12	Elliptic flow results extracted using the Scalar Product method. The measurements are reported for different multiplicity bins. . . . .	12
13	$v_2$ -coefficient for (0-20%) multiplicity bin extracted using the Scalar Product with subevents for several $\eta$ -gaps. . . . .	13
14	$v_2$ calculated with the Scalar Product with subevents $ \Delta\eta  > 0$ and without subevents in the (0-20%) multiplicity bin, shown in blue triangle and red circle markers respectively. . . . .	14
15	$\phi$ -distribution of all tracks in all events analyzed. . . . .	15
16	In the left panel the $v_2$ and $v_{2,corrected}$ for the NUA-correction are reported. In the right panel the ratio between the two is plotted. . . . .	16
17	$v_2$ -coefficient extracted using the Scalar Product with $ \Delta\eta  > 0$ for the different multiplicity bins	17
18	In the left panel the subtracted $v_2$ coefficient is shown. In the middle and right panel the $v_2$ coefficients are shown for the (0-20%) and (60-100%) multiplicity bin respectively, extracted using the Scalar Product, with $ \Delta\eta  > 0$ These two multiplicity bins are used for the subtraction. . . . .	18
19	$v_2$ -coefficients after subtraction for different $\eta$ -gaps. . . . .	19
20	$dE/dx$ for all charged particles. . . . .	20
21	$dE/dx$ for all charged particles, zoomed. . . . .	20
22	$\beta$ for all charged hadrons. . . . .	20
23	$\beta$ for all charged hadrons, zoomed. . . . .	20
24	$dE/dx$ of all pions . . . . .	21
25	$\beta$ of all pions . . . . .	21
26	$dE/dx$ of all kaons . . . . .	21
27	$\beta$ of all kaons . . . . .	21
28	$dE/dx$ of all protons . . . . .	22
29	$\beta$ of all protons . . . . .	22
30	Pion, $ \sigma_{TPC}^\pi  < 2$ . . . . .	22
31	Kaon, $ \sigma_{TPC}^K  < 2$ . . . . .	22
32	Proton, $ \sigma_{TPC}^p  < 2$ . . . . .	22
33	Pion, $ \sigma_{TPC}^\pi  < 1.5$ . . . . .	23
34	Kaon, $ \sigma_{TPC}^K  < 1.5$ . . . . .	23
35	Proton, $ \sigma_{TPC}^p  < 1.5$ . . . . .	23
36	Purity of proton [15] . . . . .	23
37	$\phi$ -distribution of all pions . . . . .	24
38	$\phi$ -distribution of all protons . . . . .	24
39	$\phi$ -distribution of all kaons . . . . .	24
40	$\phi$ -distribution of all charged particles . . . . .	24
41	In the left panel the $v_2^\pi$ and $v_{2,corrected}^\pi$ for the NUA-correction are reported. In the right panel the ratio between the two is plotted. . . . .	24
42	In the left panel the $v_2^p$ and $v_{2,corrected}^p$ for the NUA-correction are reported. In the right panel the ratio between the two is plotted. . . . .	25
43	In the left panel the $v_2^K$ and $v_{2,corrected}^K$ for the NUA-correction are reported. In the right panel the ratio between the two is plotted. . . . .	25
44	Final $v_2$ result, $ \Delta\eta  > 0.0$ . . . . .	26
45	Final $v_2$ result, $ \Delta\eta  > 0.8$ . . . . .	27
46	Final $v_2$ result, $ \Delta\eta  > 0.2$ . . . . .	27
47	Final $v_2$ result, $ \Delta\eta  > 0.4$ . . . . .	27
48	Final $v_2$ result, $ \Delta\eta  > 0.6$ . . . . .	28
49	Final $v_2$ result, $ \Delta\eta  > 1.0$ . . . . .	28